Cell-free transmission of human adenovirus by passive mass transfer in cell culture simulated in a computer model

Yakimovich, A ; Gumpert, H ; Burckhardt, C J ; Lutschg, V A ; Jurgeit, A ; Sbalzarini, I F ; Greber, U F

Abstract: Viruses spread between cells, tissues, and organisms by cell-free and cell-cell transmissions. Both mechanisms enhance disease development, but it is difficult to distinguish between them. Here, we analyzed the transmission mode of human adenovirus (HAdV) in monolayers of epithelial cells by wet laboratory experimentation and a computer simulation. Using live-cell fluorescence microscopy and replication-competent HAdV2 expressing green fluorescent protein, we found that the spread of infection invariably occurred after cell lysis. It was affected by convection and blocked by neutralizing antibodies but was independent of second-round infections. If cells were overlaid with agarose, convection was blocked and round plaques developed around lytic infected cells. Infected cells that did not lyse did not give rise to plaques, highlighting the importance of cell-free transmission. Key parameters for cell-free virus transmission were the time from infection to lysis, the dose of free viruses determining infection probability, and the diffusion of single HAdV particles in aqueous medium. With these parameters, we developed an in silico model using multiscale hybrid dynamics, cellular automata, and particle strength exchange. This so-called white box model is based on experimentally determined parameters and reproduces viral infection spreading as a function of the local concentration of free viruses. These analyses imply that the extent of lytic infections can be determined by either direct plaque assays or can be predicted by calculations of virus diffusion constants and modeling.

DOI: https://doi.org/10.1128/JVI.01102-12

Cell-free transmission of human adenovirus by passive mass transfer in cell culture simulated in a computer model

Artur Yakimovich *[1], Heidi Gumpert *[2,4], Christoph J. Burckhardt [3], Verena A. Lütschg [1], Andreas Jurgeit [1], Ivo F. Sbalzarini [2] & Urs F. Greber [1+]

* equal contribution

[1] Institute of Molecular Life Sciences, University of Zürich, Winterthurerstrasse 190, Zürich, Switzerland

[2] MOSAIC Group, Institute of Theoretical Computer Science and Swiss Institute of Bioinformatics, ETH Zürich, Zürich, Switzerland

[3] Harvard Medical School, Harvard, 240 Longwood Avenue, Boston MA

[4] present address: Center for Systems Microbiology, Danmarks Tekniske Universitet, Copenhagen, Denmark

[+] corresponding author: urs.greber@imls.uzh.ch

Running title: Live cell analyses and modeling of virus transmission

Keywords: cell lysis; multi-scale model; computational simulation; infection spreading, virus transmission

Word count text: (wo references, tables and figure legends)

Abstract:

Abstract

Viruses spread between cells, tissues and organisms by cell-free and cell-cell transmissions. Both mechanisms enhance disease by different viruses, but it is difficult to distinguish between them. Here, we analyzed the transmission mode of human adenovirus (HAdV) in monolayers of epithelial cells by wet lab experimentation and a computer simulation. Using live-cell fluorescence microscopy and replication-competent HAdV2 expressing green fluorescent protein we found that infection spread invariably occurred after cell lysis. It was affected by convection, and blocked by neutralizing antibodies, but independent of second round infections. If cells were overlaid with agarose, convection was blocked and round-shaped plaques developed around lytic infected cells. Infected cells that did not lyse did not give rise to plaques highlighting the importance of cell-free transmission. Key parameters for cell-free virus transmission were the time from infection to lysis, the dose of free viruses determining infection probability, and the diffusion of single HAdV in aqueous medium. With these parameters, we developed an *in silico* model using multi-scale hybrid dynamics, cellular automata and particle strength exchange. This 'white box' model is based on experimentally determined parameters, and reproduces viral infection spreading as a function of local concentration of free viruses. These analyses imply that the extent of lytic infections can be determined by either direct plaque assays, or they can be predicted by calculations of virus diffusion constants and modeling.

Introduction

Viral disease develops from complex interactions of viruses with their hosts during entry, genome uncoating, translation, replication, and assembly and spread of progeny viruses to uninfected cells. Spread of viruses between cells occurs by cell-free or cell-to-cell transmissions (for reviews, see 14, 72, 83). Cell-free transmissions require the dissociation of progeny particles from a producer cell, and involve large bursts of released viruses or the progressive release of smaller amounts of viruses, independent of a particular acceptor cell. This leads to viremia and enables viral spreading throughout blood fluids. Cell-cell transmissions occur at contact sites of neighboring cells. Neurotropic viruses, for example, can be transmitted between synaptic contacts of adjacent cells, and retroviruses establish new cell-cell contacts for transmission, so called virological synapses (see 23, 68, 69). For retroviruses, such as human immunodeficiency virus (HIV) or equine infectious anemia virus cell-to-cell transmission reduces the neutralization efficacy of anti-viral antibodies and anti-viral drugs (66, 91, 113). This illustrates that viral transmission modes modulate the efficacy of immune defense, and they impact on anti-viral strategies, such as vaccine design and the development of new anti-viral compounds.

Little is known about lytic cell-free transmission of viruses, although it occurs with both non-enveloped and enveloped viruses, and is key for clinical efficacy of oncolytic viruses (57, 78, 111). Theoretical calculations considering the rate of viral production, life-span of the producer cell and the neutralizing capacity of antibodies have suggested that the lytic life cycle with large burst-sizes promotes survival in the face of antibody attack (51). The lytic cycle can be modulated by the replication rate, and thereby avoid extinction of the host cells and dilution of the virus (114). Accordingly, viral strains with variable replication rates coexist rather than dominate one another. This is illustrated by persistent non-enveloped lytic viruses *in vivo* and in cell lines, for example poliovirus (22), coxsackievirus (100), foot-and-mouth disease virus (24), reovirus (1) or human adenovirus (HAdV, 33, 101).

HAdVs replicate in experimentally infected people, and are transmitted between individuals (59). They cause infections with epidemic, endemic or sporadic

disease and viremia or massive viral excretions (73, 89). Currently, there are 57 HAdV types grouped in 8 species, including a recently discovered zoonotic TMAdV (18). More than one third of HAdVs are associated with disease in the respiratory, digestive, excretory and ocular systems (44, 55, 71). Fatal cases of HAdV infections were reported from immunosuppressed patients due to T-lymphocyte deficiencies (52), while infections in immune-competent individuals are usually self-limiting.

HAdVs have a diameter of about 90 nm and a double-stranded DNA genome of 36 kb, but no envelope (7, 61, 82). The protruding fibers mediate virus attachment to cellular receptors. These receptors include trans-membrane proteins, such as the coxsackievirus adenovirus receptor (CAR), membrane cofactor CD46 or desmoglein-2, or glycans (8, 32, 75, 92, 105, 108). Infections with HAdV2 (short Ad2), HAdV3 or HAdV5 (short Ad5) are enhanced by integrin coreceptors, which bind to the penton base protein on the viral capsid (2, 60). CAR and integrins are localized on the basolateral and junctional membrane of polarized epithelial cells, facing away from the airways of the lungs. These receptors can be redirected to the apical surface by virus stimulated macrophages and cytokine signaling, and thereby provide a vital passageway for the viruses into the epithelial cells (63). Downstream of receptor binding, Ad2/5 engages drifting motions on CAR and is confined by integrins (15). Drifts and confinements trigger the first steps in the uncoating program, the loss of the fibers and exposure of the membrane lytic protein VI (15, 39, 112). This is followed by receptor-mediated endocytosis (70), and enables virus escape from endosomes (34). The cytosolic viruses traffic on microtubules using the dynein/dynactin motor complex to reach the nucleus (12, 29, 35, 54, 99). They dock to the nuclear pore complex, disassemble by a kinesin motor-mediated disruption process, and release the viral genome into the nucleus (98, 106). In the nucleus, they initiate the replication program by transcribing the immediate early activator proteins of the E1 region encoding E1A and E1B proteins, which are essential to drive the expression of all other viral proteins (10). The formation of progeny particles in the nucleus requires the replication of the viral DNA, and structural viral proteins from the major late transcript (reviewed in 9).

While there is experimental evidence for lytic and non-lytic egress of Ad5 (102), the mechanisms of lytic viral release and spread from infected cells are poorly

understood. Proteolytic cleavage of cytokeratin K18 by the viral protease is thought to reduce the mechanical stability of the cytoplasm, and facilitate viral release (20, 65). In addition, the release of Ad2/5 is facilitated by the adenovirus-death protein 11.6 kDa encoded in the early region 3A (E3A) (102). Although encoded in E3, the 11.6 kDa protein is expressed at very low levels in the early phase of infection, and at very high levels late in infection from the major late promoter (103).

The early region 3B does not directly affect the replication cycle of the virus. It encodes three proteins, which protect the virus from host anti-viral responses in acute infections (58). These proteins antagonize cell death triggered by cytotoxic lymphocytes or cytokines released by activated macrophages. Two E3B proteins, 10.4 kDa and the 14.5 kDa, form the receptor internalization and degradation complex (RID). RID triggers endocytosis and lysosomal degradation of the Fas receptor and TRAIL receptors 1 and 2 (reviewed in 9). The third open reading frame in the E3B region is the 14.7 kDa protein. It inhibits tissue necrosis factor (TNF) alpha (36), TRAIL (104) and Fas ligand induced apoptosis (19) by binding to a caspase downstream of the receptors. This protein also blocks NFkB signaling, which is crucial for anti-viral immunity (reviewed in 9).

HAdV egress from an infected cell in a multi-cellular environment has not been quantitatively described so far. Here, we developed a multi-scale hybrid dynamics model using a cellular automaton and particle strength exchange based on experimentally determined parameters. Computational models have been developed to study viral propagation between cells, typically based on ordinary differential equations (11, 79, 97). Cellular automata (CA) have been used to study viral infection spread, because of their natural discreteness and the ability to resolve spatial localization (6, 50, 115). They were used to model virus spread in cell culture, albeit without quantifying diffusion dynamics and accounting for bulk currents (4). While CA are useful for the discrete modeling of cell behavior, they are not very suitable for modeling virus particle diffusion in the extracellular space. To relax limitations of discreteness and dimensions, hybrids of established modeling approaches were developed (64). Our hybrid spatio-temporal model for the propagation of HAdV infection combines CA with a partial differential equation formalized by a particle strength exchange (PSE) method (25) to describe diffusion of viruses in the cell-free environment. We show that passive mass transfer of

released HAdV progeny in the cell-free environment is sufficient to explain the dynamics of HAdV infection spread in monolayers.

Materials and Methods

Cell culture and viruses

Human lung carcinoma A549 (HLC-A549) cells were purchased from American Type Culture Collection (Rockville, MD, USA). Early region 1 (E1) transfected HER-911 cells (31) were grown as monolayers in Dulbecco's modified Eagle medium (DMEM) supplemented with 10% fetal bovine serum (FBS, GIBCO-BRL) on cell culture dishes or 96-well plates (Matrix, Thermo Fisher Scientific, Lausanne, Switzerland).

Ad2-dE3B-GFP was constructed in *E. coli* strain SW102 by mutagenesis of a bacterial artificial chromosome (BAC53) carrying the entire Ad2 genome and the phage lambda recombineering genes, which allowed for a 2-step GalK positive selection and deoxy-galactose counter-selection as described earlier (46, 48, 81, 109). The E3B genes were excised at the end of the E3A poly-adenylation site (nucleotide 29780) and before the E3B poly-adenylation site (nucleotide 30841), and replaced by GalK using the following primer pair: 5' gaaaccatgttctcttctttacagtatgattaaatgagaccctgttgacaattaatcatcggca 3' and 5' gctggacaaagatttgctgactgattttaagtaagtaatttattgtcagcactgtcctgctcctt 3'. The eGFP open-reading frame controlled by a CMV promoter and an SV40 termination site of 1642 bp was inserted in place of GalK using the following primer pair: 5'gaaaccatgttctcttctttacagtatgattaaatgagactagttattaatagtaatcaattacggggtc3', 5'gctggacaaagatttgctgactgattttaagtaagtaatttattgttaagatacattgatgagtttggacaaacc3'. The final BAC construct was verified by DNA sequencing using primers in the E3A and the E4 region, and found to be correct (not shown). Ad2-E3B-eGFP BAC DNA was purified using a Maxi preparation kit (Sigma), linearized by *Dpn I* restriction, phenol-chloroform extracted, ethanol precipitated and transfected into 293 cells by calcium phosphate precipitation. Virus particles were grown in HLC-A549 cells, and purified by double caesium chloride gradient centrifugation. Ad2-

E3B-eGFP was found to be homogeneous by SDS-PAGE and transmission EM negative stain analyses (not shown).

For time-resolved infection studies, purified Ad2-dE3B-GFP was added to A549 cells at $5 \cdot 10^{-7}$ mg/ml protein, about 3 particles per cell. From the protein concentration measured in the purified virus preparation, we determined a theoretical number of adenovirus particles (TNAP) according to equation (1)

$$TNAP = \frac{\text{viral protein concentration } (\mu g/\mu l)}{\text{viral protein mass } (\mu g)} \qquad (1)$$

The mass of one virus was assumed to be $2.5 \cdot 10^{-19}$ kg, about 150 MDa (107).

Transgenic Ad2-dE1-GFP was generated by ET recombination mediated insertion of a CMV promoter GFP expression cassette to the E1 region of Ad2 (nucleotides 461-3510). BAC-DNA was verified for correct insertion of the GFP gene, purified and transfected into HER-911 cells for virus growth as described (81). Ad2, Ad2-dE3B-GFP and Ad2-dE1-GFP were grown, isolated and in case of Ad2-Atto488 dye (ATTO-TEC, Germany) as described (15, 31, 38, 74). Protein concentrations of purified viruses were measured using the PIERCE Micro BCA protein assay reagent kit (Thermo Fisher Scientific, Lausanne, Switzerland).

Automated cell segmentation and infection probability calculations

Automated cell segmentation was performed computationally using CellProfiler 2.0 software (16). Analysis involved custom-made CellProfiler 2.0 pipeline involving thresholding of multiple signal source images. Thresholding efficiency was calibrated visually for each dataset. Results from automated cell segmentations were used to count GFP positive cells 72 hpi. These values were used to calculate the fraction of infected cells depending on input virus concentration. These data were used to calculate the probability of infection.

From the protein mass of an individual HAdV particle (107) we defined TNAP using equation (1). From the fraction of GFP-positive cells calculated, we determined the infection probability depending on the amount of input virus and

normalized the probability over the typical length of an experiment, which was 72 h. We assumed that the majority of the particles attached onto the cell monolayer during this period. This allows us to calculate the impact of TNAP per arbitrary area unit on the probability of infection.

Complementary co-cultures of HER-911 and HLC-A549 cells

HER-911 and HLC-A549 cells were grown to 95% confluence in separate wells of a 96-well plate. HER-911 cells were inoculated with Ad2-dE1-GFP (MOI 10^4, 0.053 µg/µl) in DMEM containing 2% BSA at 37°C for 1 h, washed 3 times with PBS, stained with CellMask deep red dye (Invitrogen) and detached with Accutase (Sigma-Aldrich) at 37°C for 7 min. Singular HER-911 cells were re-suspended in DMEM containing 10% FBS, diluted 1:800 with DMEM-FBS and added to a monolayer of HLC-A549 cells. Infection was imaged 24 hpi as described below. The co-occurrence of CellMask and GFP dyes was quantified by cell segmentation with CellProfiler 2.0.

HAdV neutralization

Ad5 was incubated with an Ad2/5 neutralizing antiserum (kindly obtained from Dr. Anja Ehrhardt, 43) in 96 well dishes containing 50 µl of DMEM and 1% BSA. HLC-A549 cells were added to the wells, incubated at 37°C for 7 days, fixed and stained with the cell-dye crystal violet dye (0.25 mg/ml crystal violet in H_2O containing 5% EtOH.

Semi-solid medium

Semi-solid medium was prepared using cell culture grade ultra-low melting agarose, type VII (SIGMA, Fluka, Buchs, Switzerland). Agarose was dissolved in PBS at 3 mass percent. This concentrated gel was heated up to 90° C in a microwave oven, cooled down, controlled for water loss and precise agarose concentration using gravimetry, volume adjusted by addition of H_2O, diluted with warm cell growth medium, and overlaid on top of the cell monolayers or used for diffusion measurements of purified fluorophore tagged HAdV particles.

Time-lapse multi-site multi-channel microscopy

Time-lapse multi-site multi-channel microscopy images were recorded with an automated ImageXpressMICRO fluorescence microscope (Molecular Devices, Munich) using 10x Nikon S Fluor objective with 0.5 NA, and equipped with a humidified chamber at 37° C and multiple wavelength excitation/emission filters (Semrock). All live imaging experiments were performed in 96-well black plates (Matrix, Thermo Fisher Scientific, Lausanne, Switzerland). For image acquisitions cultured cells were maintained in 20 mM Hepes buffered bicarbonate-free Roswell Park Memorial Institute 1640 medium (RPMI, GIBCO-BRL) supplemented with 10% fetal bovine serum (FBS, GIBCO-BRL) and penicillin-streptomycin (GIBCO). Image acquisition at multiple sites was enabled with a motorized stage allowing precise high speed selection of regions of interest within a well. Using MATLAB (Mathworks, Natick, Massachusetts, USA) based post-processing, images were stitched into pictures of high resolution covering roughly 85% of a 96 well in case of experiments involving plaque (PQ) analyses. This allowed analyses of virus infection spreading over large areas with high resolution.

Imaging of HAdV particles and fluorescent beads

The movements of adenovirus particles and fluorescent beads was imaged using custom made total internal reflection fluorescence (TIRF) microscopy based on an Olympus IX81 inverted microscope equipped with a Cascade 128+ camera (Photometrics, Roper Scientific, USA), 100x 1.45 NA oil immersion PlanApo (Olympus) objective and a custom made thermostatic chamber (15). Yellow-green Fluoresbrite fluorescent beads size range kit used was purchased from Polysciences (USA). Microscopy was performed at 37° C. The TIRF angle was manually adjusted in each case in order to obtain the optimal signal-to-noise ratio. The image acquisition was controlled by Metamorph software (Molecular Devices, Visitron Systems, Germany). For the measurements we used type I ultrapure water (18.2 M Ω/cm) and live imaging medium (Imaging medium). Imaging medium had the following composition: Hank's Buffered Salt Solution (HBSS), 0.2% Bovine serum albumin (BSA, SIGMA), 1 mg/ml ascorbic acid, optional 10% FBS (or without addition of 10% FBS in the case of low serum imaging medium).

Measurements were conducted in media containing different concentrations of agarose. Movies with a high time resolution (0.001 s/frame) were acquired and used to track individual HAdV particles. Particle tracking was performed with the "particle tracker 3D" plugin in ImageJ (86). The resulting trajectories were used to compute HAdV diffusion constants from the moment scaling spectrum as described (30, 37).

Measurement of the HAdV diffusion constants

The diffusive properties of HAdV particles were determined using high speed TIRF microscopy of fluorescently labeled viruses at 1000 Hz acquisition frequency, and single-particle tracking in 2-dimensional mode using the "particle tracker 3D" ImageJ plug-in (86). Viral trajectories were used to compute diffusion constants from the moment scaling spectrum slope. The procedure was calibrated using various sized fluorescent beads and compared to values predicted by the Einstein-Stokes equation (2).

The diffusion constant (*D*) of a given particle can be calculated theoretically or measured experimentally. Theoretical values of diffusion constants for ideal spherical particles can be predicted using the Einstein-Stokes equation

$$D = \frac{k_B T}{\pi \eta r} \qquad (2)$$

where *D* is the diffusion constant, k_B Boltzman's constant, *T* the temperature, η the viscosity of the environment, and *r* the hydrodynamic radius of the particle.

Determination of the mode of diffusive motions

To confirm the validity of the theoretically calculated *D* values from equation (2), we characterized the motion mode of the fluorescent beads by estimating the Reynolds number (*Re*). *Re* is a measure of the ratio of inertial forces and viscous forces acting on the particle. Equation (2) assumes laminar Stokes flow and is only valid for *Re* much smaller than 1. In our system we estimated *Re* for Brownian motion of various-sized beads ranging from 38 to 1000 nm (Table 1). All

values of *Re* were smaller than 0.1, suggesting laminar motion (28), and justifying the use of equation (2) for HAdVs. Equation (2) is also valid for most of the currently known globular virus particles.

Computation of the Reynolds number for fluorescent particles

To confirm the validity of theoretically calculated diffusion constants using equation (2), we estimated the Reynolds numbers (*Re*) for Brownian motion of beads ranging from 38 to 1000 nm in diameter. Equation (2) is only valid if the flow of medium around the diffusing virus particle is laminar (28), which is the case for *Re* much lower than 1.

Re can be computed using equation (3):

$$Re = \frac{\rho V L}{\eta} \qquad (3)$$

Where ρ is the density of the fluid, η the dynamic viscosity of the fluid, V fluid velocity, L diameter of the spherical particle. L for the fluorescent beads were purchased from Polysciences (USA). η for distilled water at 37°C was computed from equation (4):

$$\eta = A \cdot 10^{\frac{B}{T-C}} \qquad (4)$$

where A = 2.41·10^{-5} Pa·s, B = 247.8 K, and C the fluid temperature in degree Kelvin. ρ for distilled water at 37°C is 991.27 kg/m^3.

Fluid velocity estimations around the Brownian particle (V) can be obtained using several approaches. For example, it could be measured experimentally, although this is limited by the temporal resolution. From our experimental measurements, we computed two types of V, instantaneous speed (V_{inst}) and mean speed ($\langle V \rangle$). The trajectories from the 1000 Hz TIRF microscopy experiments were used to estimate V_{inst}, while $\langle V \rangle$ was computed from experimental D values according to equation (5):

$$< V > = \sqrt{\frac{2D}{t}} \qquad (5)$$

where *t* is the time length of the trajectory.

To control for potential underestimations of *V* values from experimental data we computed theoretical instantaneous root mean square velocity values (V_{RMS}) from equation (6) according to (56)

$$V_{RMS} = \sqrt{\frac{k_B T}{m}} \qquad (6)$$

We then computed *Re* based on maxima of V_{inst} , <*V*> and V_{RMS}. All values of *Re* obtained were smaller than 0.1 (see Table 1), which allowed good theoretical predictions of diffusion constants for spherical particles using equation (2). Furthermore, the size range over which we calibrated the method covered most currently known viruses, which allows equation (2) to predict diffusion constants for many other globular virus particles.

Description of the computational model

The computational model was developed using MATLAB 2010a (The MathWorks, Natick, MA, USA). The model consists of a CA and a PSE module. The CA is a discrete module composed of a grid of cells, each of which in a defined state and conforming to rules that are updated according to the present state of the cells. PSE is a deterministic particle method to simulate diffusion.

The implemented CA uses a hexagonal grid to represent biological cells. The state of the cell describes their infection status and viability. The time step for the CA is 1 h, sufficient to resolve key events, such as cell infection and lysis. At each time step, the status of the cell is checked and updated if required. A lysis clock is also updated if the cell state is currently in productive infection mode. The hexagonal CA grid consisted of 200 x 231 cells, 46,200 cells in total. The size of each cell was 24 μm and the total layer of cells 4812 x 4808 μm^2.

The state of each cell can be uninfected, dead, infected, or non-lysable. All cells are uninfected at the beginning of the simulation, except for one initially infected cell. An uninfected cell can die or be infected or non-lysable. The proportion of dead cells over the course of the biological experiment was calculated. Uninfected cells were chosen randomly to die during the simulation in order to match the ratio obtained from the biological experiments. An uninfected cell may be infected based on an experimentally determined probability depending on the local concentration of virus. Between different CA time steps, the maximum TNAP concentration was recorded for each cell. This concentration was compared with the probability of infection at the appropriate virus concentration. A random value of 0 or 1 was used to determine if the cell becomes infected by comparison to the experimentally obtained probability of infection. Probabilities of infection between experimental concentrations were linearly interpolated, based on the experimental observation that not all the infected cells went on to lyse and form PQ. As soon as a cell was infected, this cell was randomly assigned to either proceed to a lytic or a non-lytic infection, based on experimentally determined probabilities of infected cell lysis. As soon as a cell was infected, a lysis clock was initiated which then determined the time to lysis from a uniform distribution taken after the first infected cells were observed to lyse between 1 and 5 days pi (dpi). The level of GFP intensity in lytic or non-lytic infected cells was taken as an indicator for the progress of infection. The GFP intensity signal increased over time as determined by linear extrapolation between calculated virus concentrations. The GFP intensity values can be linearly interpolated until selected maximum virus concentrations measured in the biological experiments for experimental purposes. The PSE diffuses the virus particles released from an infected cell. The time step of the PSE is set to satisfy the forward Euler stability criteria, $dt < h^2/2D$, where h is the space between particles, and D the diffusion constant. The PSE module stopped running when the local concentration of virus was below the infection threshold. As a result of multi-scale nature of the CA and PSE components of the hybrid model in temporal dimension, the PSE module runs between time steps of the CA. As mentioned above, the maximal concentration of virus the cell is exposed to between individual CA steps is tracked during the course of the PSE module execution. The PSE was implemented as described in (25). Particles were placed on a regular grid and the number of particles used was chosen such that approximately nine particles gave support to one CA cell. A cloud-in-cloud

assignment scheme was used to add virus to the PSE module after cell lysis, and to determine the local concentration of virus at each cell.

Radial distribution function for plaques

A method to determine the radial distribution function (RDF) of intensity was developed to characterize the PQs in biological and *in silico* experiments. The input for the method was an image (intensity matrix), as well as the user defined center of the PQ. The perimeter of a PQ was scanned by single degree resolution, and GFP intensities projecting around the center were averaged in concentric rings with a width of 1 pixel (0.645 μm) with 0 pixels spacing. The average intensity from each ring yielded the RDF values. The center of biological PQs was determined by user input, while the center of *in silico* PQs was taken as the initially infected cell.

Experimental and simulated time resolved plaque formation

Individual PQs from Ad2-dE3B-GFP infected HLC-A549 cells were imaged by live cell fluorescence microscopy in hourly intervals as described above, and radii of PQs fitted using ImageJ software. The simulation of PQ formation was performed using the parameters described above.

Results

Ad2 infection visualized in epithelial cell monolayer

We used ET mutagenesis (81) to engineer a replicating, E3B-deleted Ad2, which expresses the GFP reporter in the E3 region from the major cytomegalovirus promoter (short Ad2-dE3B-GFP). This virus was fully replication competent, and developed plaques similar in appearance and size in human airway epithelial lung carcinoma A549 cells (HLC-A549) as Ad2 (Fig. S1). Live cell, multi-site time-lapse microscopy showed that inoculation of Ad2-dE3B-GFP led to sporadic occurrence of GFP-expressing cells in the monolayer, indicating infection. About 2-3 dpi,

larger zones of GFP-positive cells developed around initially GFP-expressing cells. We termed these foci plaques (PQ), although in a strict sense they are 'spreading phenotypes', an example of which is shown in Fig. 1A and B. Our PQs resemble classical viral plaques, which were introduced more than 60 years ago enabling the first systematic and quantitative measurements of viral infections (27). To visualize cell lysis we used propidium iodide (PI), a positively charged cell-impermeable phenanthridine dye, which intercalates with double-stranded DNA and RNA and upon binding emits 20-30 fold enhanced orange-red fluorescence at 617 nanometers compared to the free dye (96). The PI signal can only be observed if the plasma membrane is broken. The transition of a GFP-positive cell to a PI-positive cell occurred faster than the 1 h resolution used in these experiments, that is, it appeared in the frame following the initial GFP signal. For the 10 analyzed PQs the transition from an initially infected cell to a PQ usually occurred 4 to 14 h after cell lysis (Movie S1).

We calculated the probability of a PI signal to occur at the time point of the GFP-PI transition event, and the geometrical probability of this event to occur inside a circular area large enough to contain both the source of the GFP signal and the PI signal. The probability of a double positive GFP and PI-stained cell was less than 1 in a thousand ($P = 0.00045 \pm 0.00025$, $N=10$). We conclude that Ad2-dE3B-GFP inoculation leads to a sequential order of events suitable for live cell image analyses, initial infection monitored by intense GFP expression, cell lysis by PI staining, and secondary infections of neighboring cells, which gives rise to a PQ.

HAdV infection spread involves cell-free virus particles

To test if PQs depend on the release of free progeny viruses into the medium, we tested if convection influenced the shape of the PQs. Convection is a macroscopic description of heat and mass transfer in fluids, and consists of advection and diffusion (49). Advection results from bulk fluid motions caused, for example, by local temperature differences. Advection is cancelled in gels by the frictional forces between the liquid and the polymer network (17). PQs with comet-like shapes were observed in liquid medium, and circular shapes in semi-solid medium (Fig. 2A, B, and Movie S2). In both cases, the GFP signal was more intense in the center of the PQ than the periphery. The strong influence of advection on the development of PQs was underscored by the observation that

the comet-shapes were uniformly directed uphill in tilted plates, while they were randomly positioned in horizontal plates in liquid medium (Fig. S2). In gelled medium, the PQs were largely symmetrical presumably due to dissipation of advection currents caused by friction.

To test if infection spreading involved extracellular viruses, we used an anti-Ad5 neutralizing serum (43). At 1:10 but not at 1:500 dilutions, it blocked single round Ad2-dE3B-GFP infection of HLC-A549 cells by about 10-fold (Fig. S3A). At 1:30 dilution, it neutralized Ad5 infection of HLC-A549 cells by end point titration assays at 10^4 or less viruses per cell (Fig. S3D). Higher amounts of antiserum were effective also against 10^5 Ad5 per cell, confirming the high neutralization potency.

We next inoculated HLC-A549 monolayers in 96 wells with Ad2-dE3B-GFP ($5x10^{-7}$ µg/µl, 3 particles per cell), removed the inoculum 24 hpi, covered the cells with medium containing neutralizing antiserum and observed the infection by live cell GFP imaging. At the 1:10 dilution of the serum, we observed one PQ per well, and 3.5 PQs at 1:500 dilution (Fig. 2C, and Movie S3). Untreated cells or cells treated with heat-inactivated antiserum had an average of about 5 PQs per well, and these PQs were larger than the PQs from cells treated with neutralizing antibody. The data show that most PQs were blocked by the neutralizing antiserum indicating that extracellular Ad2 drive PQ formation. A small fraction of PQs was resistant to the antibody. Since PQs only formed from lytic infected cells, this suggests that a small amount of extracellular viruses were not recognized by the antiserum. PQ formation, however, depended on passive transfer of infectious viruses in the medium, influenced by bulk liquid motions. These motions comprise advection and diffusive mass transfer. In subsequent experiments, we restrict HAdV mass transfer to diffusion with semi-solid medium.

Lysis of a single cell leads to the formation of a plaque

If HAdV spreads to neighboring cells by passive mass transfer, a single infected cell should produce a PQ. We tested this hypothesis in a co-culture system of infected human embryonic retinoblast 911 cells (HER-911), which replicate E1-deleted Ad2 expressing eGFP (Ad2-dE1-GFP). Low amounts of infected HER-911 were seeded onto uninfected HLC-A549 acceptor cells, which can be infected but do not replicate Ad2-dE1-GFP, and thereby allow for a single round of infection

(Fig. S4). Live cell, multi-site time-lapse microscopy revealed GFP-positive HER-911 donor cells 54.5 hpi, followed by lysis of one of the donor cells, and the formation of a PQ in HLC-A549 cells at 104.5 hpi (Fig. 3). These PQs were similar in size as those observed with replicating Ad2-dE3B-GFP in HLC-A549 cells, and they depended on donor cell lysis and advection (Fig. S5). We noticed a significant amount of dead cells at late imaging time points of both infected or uninfected cells (see Fig. 1 and Fig. 3). This was most likely due to imaging-induced photo-toxicity. The lysis clock was modeled by a uniform distribution probability. An exponential distribution probability gave similar results (not shown). Importantly, in the wet lab experiment, imaging did not affect the size of PQs up to 3 days pi, as concluded from PQ analyses without intermittent imaging, in agreement with our simulations using different lysis clock probabilities (data not shown). Together, the data indicate that viruses spread from a single lysed cell in the absence of lytic viral replication in the acceptor cells.

The foundations of a model for lytic spread of HAdV

To quantitatively characterize the spreading of HAdV infection by a cell-free mechanism we developed a novel computational model (for overall workflow of the model and the cell state flowchart, see Fig. 4). The model hybridizes a cellular automaton (CA) with particle strength exchange (PSE). PSE is a mesh-free method to simulate diffusion, and is used here to simulate the diffusion of viral particles after cell lysis.

The CA represents the geometry of a monolayer composed of a grid of hexagonal digital cells representing the biological cells. The CA also tracks the states of all cells, that is, uninfected, infected, infected and non-lysable, or lysed. Uninfected cells can become infected with a certain probability depending on the viral particle concentration at the location of the cell. In addition, not all cells that are infected also lyse and release infectious viruses. In our model, the productively infected cells were assigned an internal clock, which determines when they lyse. The lysis clock starts to tick upon infection, and the expected lysis time is sampled from a uniform distribution between 1 and 5 dpi, as determined from our previous observations (Fig. 1, Movie S1), in agreement with data from the literature (102). When the clock indicates that a cell should lyse, the emerging viral particles are

locally added to the PSE simulation using a 'cloud-in-cell' assignment scheme (47). The PSE then diffuses the viral particles between time steps of the CA.

To enhance the relevance of the model, we included the following experimentally determined parameters: i) the average size of a cell, ii) the time lag for an infected cell to lyse, iii) the probability for a GFP-positive cell to lyse iv) the diffusion constant of HAdV in the extracellular medium, v) the probability of infection as a function of local virus concentration vi) the GFP intensity increase rate after infection and vii) the probability of cell death for uninfected cells (Fig. 5). The only parameter obtained from the literature was the amount of viral particles released from a lysed cell. It was estimated that one HAdV-infected cell releases 100,000 to 200,000 viral particles (40, 77). For the sake of simplicity we used 100,000 in our model, unless specified differently.

i) Average size of a cell. Our CA model uses a uniform hexagonal cell grid. The cell size was calculated from the average number of Hoechst-stained nuclei on a given area from near confluent cells (see Fig. 1B). Assuming that the approximate cell shape is a hexagon, we computed the inner radius (r) of the hexagon from the average cell area (A) using the formula: $A = 2\sqrt{3}\cdot r^2$. The calculated average radius of a cell was 12±1 µm, which is in excellent agreement with direct cell measurements of cell size (data not shown).

ii) Time for an infected cell to lyse. Since cell lysis triggers secondary infection rounds, it is important to accurately estimate this parameter of the model. According to earlier reports, HAdV-infected cells are expected to lyse 1 to 5 dpi (102). Using live cell imaging of PI, we observed that infected cells started to lyse 1 to 2 dpi with a uniform probability distribution up to 120 hpi (Fig. 1, Movie S1).

iii) The probability for an infected cell to lyse. We observed that for unknown reasons not all GFP-positive infected cells lyse and produce a PQ within 5 dpi. The ratio between the numbers of PQs developed within 5 days and the number of GFP-positive cells before development of PQs (24 hpi) was 7.4±1.2%.

Based on these findings, we defined that an infected cell can lyse with a probability of 0.074 during the 5 days time window. The probability that an infected cell enters a "non-lysable" state was hence 0.926.

iv) Diffusion constant of HAdV in the extracellular medium. The diffusion constant (*D*) of a given particle can be calculated theoretically or measured experimentally according to equation (2). HAdV particles have a complex shape. The icosahedral capsid is approximately 90 nm in diameter, and contains 12 fibers, which project away from the capsid by about 37 nm (61). If Ad2 were an ideal sphere, *D* would be between 4.06 $\mu m^2/s$ and 7.31 $\mu m^2/s$ for particles with and without fibers, respectively. We experimentally determined *D* for Ad2 by total internal reflection fluorescent (TIRF) microscopy of Ad2-atto488 and single-particle tracking analyses using spherical fluorescent beads as internal standards. Comparison of the experimental *D* values for these beads in cell growth medium, water or agarose with theoretical values from equation (2) indicated good overall correlations, suggesting that our experimental procedures were valid (Fig. S6A, B). The experimentally determined $D_{Ad2\text{-}atto488}$ of 6.47±19.45 $\mu m^2/s$ in medium was well within the range of the theoretically predicted values from equation (2). Equation (2) was valid, since our experimental setup involved mostly laminar Stokes flow, as indicated by the computed Reynolds numbers, which were far below 1 for beads from 38 to 1000 nm (Table 1, and materials and methods). As expected, $D_{Ad2\text{-}atto488}$ was dependent on the concentration of agarose in the semi-solid medium (Fig. S6C). At agarose concentrations above 3%, $D_{Ad2\text{-}atto488}$ dropped below the values in pure solvent or agarose less than 3%, consistent with the diffusive behavior of particles in gels with mesh sizes larger than the particles.

v) Probability of infection as a function of local virus concentration. In order to fix the infection probability parameter in our model, we measured the relationship between the concentration of input Ad2-dE3B-GFP and the probability of infection of HLC-A549 (Movie S4). The proportion of infected cells determined by automated computational cell segmentation using CellProfiler (16) increased with increasing amounts of virus 72 hpi (Fig. 6A). Similar results were obtained with Ad2-dE1-GFP (Fig. S7A). Based on these values, we determined how the infection probability depends on input virus. To obtain the probability of infection for every CA time step at 1 h sampling frequencies we used the empirically determined distributions of probabilities at the local virus concentration over 72 h. This approach allowed accounting for the threshold TNAP needed for the successful infection of an individual cell. We thereby took into account potentially

non-infectious virus particles and all particles that fail to successfully deliver their genome to the nucleus. The entire infection process was lumped into a single probability, which depends on the amount of input virus.

vi) GFP intensity rate increase after infection. There was a difference in GFP intensity between the center of a PQ and its periphery (see Movie S1 and Fig. S2). A similar difference in intensity could be observed when cells were infected with different amounts of virus (see Movie S4). To quantify this intensity difference cell monolayers were infected with different concentrations of Ad2-dE3B-GFP, and the mean GFP intensity (averaged per well) measured for each virus concentration as a function of time (Fig. 6B). We found that the signal-intensity difference correlates with the amount of Ad2-dE3B-GFP used for infection. The obtained values were used to simulate GFP signals in the model. Similar measurements were also carried out and simulated for Ad2-dE1-GFP (Fig. S7B). In summary, the correlation of input virus and intensity of infection allows setting the corresponding kinetic parameters in the model.

vii) Probability of cell death for uninfected cells. Since dead PI-positive cells cannot be infected, we determined the amounts of dead cells as a function of time. Particularly towards later time points of infection imaging, we observed a significant number of GFP-negative cells turning PI-positive (Fig. 1, Fig. 3, Movie S1). This was independent of infection, as indicated by comparison of the number of PI-positive cells in infected and non-infected wells (Fig. 6C). The observed cytotoxicity is most likely caused by limiting cell culture and fluorescence imaging conditions. Based on the appearance of PI-positive cells over time, we computed the probability for an uninfected cell to lyse, and incorporated this into our model.

In silico and biological plaques have similar features

We next ran the hybrid CA-PSE model for Ad2-dE3B-GFP infection with the parameters described above and analyzed its output for PQs. We compared 15 *in silico* PQs with 15 biological PQs. The patterns predicted by the model resemble those of the biological PQs, including features, such as non-infected cells inside the zone of PQs and out-lying infected cells (Fig. 7 and Movie S5).

Using CellProfiler and custom-made software, we measured a number of phenotypic parameters of biological and *in silico* PQs, such as the mean radius,

the mean number of infected and non-infected cells, and the mean speed of the spreading front, which was computed from the average change of radius over time. The average values of these parameters taken from 15 biological and *in silico* PQs are listed in Table 2. The radii and the speeds of the spreading front of biological and *in silico* PQs were qualitatively similar, while there were small differences in the number of total cells and the number of infected cells within PQs. Since both of these phenotypic features depend on the cell shape, we believe that the observed difference is due to the model assuming a uniform hexagonal grid with all cells having the same shape and size. The model does not account for biological cell-to-cell variability, which can be due to cell division or migration. We conclude that the model has a good overall ability to predict non-geometric phenotypic features of PQs, and their emergence and propagation.

Radial distribution function for quantitative model validation

We next validated quantitative fluorescence intensity distributions of individual cells within zones of PQ predicted by the model. To measure changes of the signal intensity from the center of a PQ to the periphery, we used a radial distribution function (RDF). This renders the read-out invariant to sample rotation, a suitable feature of radially symmetric PQs. The RDF quantifies the average fluorescence intensity as a function of distance from the center of a PQ, obtained by averaging the fluorescence intensity along concentric circles (45). We first measured the RDF of a PQ from single-round infections with Ad2-dE1-GFP. As indicated in Fig. 8A, the RDF captures the visually observed intensity decreased with distance from the PQ center. In addition, the distance-dependent decrease of GFP fluorescence intensity, observed in both experimental and simulated RDFs quantitatively reflected the signal intensity observed in individual cells of biological PQs. The RDF intensity profile is hence a useful tool to compare *in silico* PQs and biological PQs, in particular if RDFs from multiple PQs are averaged to iron out the inherent noise in both *in silico* and biological PQs.

The virus concentration gradient determines the size of plaques

Next, we compared the RDFs from experimental PQs and simulated PQs using replicating Ad2-dE3B-GFP. From averaged 15 experimental and 15 independent

simulated PQs we found that the intensity decrease of infection was similar in both cases, and was strongly dependent on the distance from the PQ center (Fig. 8B, C). We conclude that the distance-dependent intensity decrease of infection is a general feature in PQs of both replicating and non-replicating HAdVs. Our model showed that this distance-dependent intensity decrease was caused by a concentration gradient of free virus particles formed as a result of virus release from an infected cell and free diffusion of virus in the medium. We suggest that this mechanism is responsible for the distance-dependent intensity decrease in the biological system.

High local virus concentrations lead to hyper-infection

The averaged biological and *in silico* RDFs had a good overall fit of the GFP intensities. For example, the fluorescence intensity dropped to half of the center value at about 4 cell diameters (150 µm) from the PQ center in both cases. We hypothesized that the significant difference between the GFP intensity in the center and the periphery could be due to a local hyper-infection of cells (MOI much larger than 1) with Ad2-dE3B-GFP or Ad2-dE1A-GFP in close proximity to the lysed donor cell in the center. We simulated conditions to suppress the impact of hyper-infection on the simulated GFP intensity. For this, we fixed the maximum GFP intensity that could be reached by a simulated cell to experimentally measured average GFP intensity obtained with virus concentration of 0.05 µg/µl (MOI 10^4). Here virus concentrations higher than 0.05 µg/µl have the same impact on the level of GFP intensity as the concentration of 0.05 µg/µl. (see Fig. 6A). Under these conditions, the GFP intensity peak around the PQ center disappeared from the simulated RDF (Fig. 8D), in contrast to the non-restricted simulation (Fig. 8C). We concluded that the high level of infection in the closest proximity of the lysed cell was the result of a high local concentration of released virus particles, leading to local hyper-infection.

An estimation of the number of released virus particles

The number of released virus particles from infected cells may vary from cell to cell. Population values for virus particles produced per cell center around 100,000 (40, 77). We computed different RDFs for different numbers of released particles,

and averaged them from 15 *in silico* simulations (Fig. 8E). As expected, the RDF intensity increased with increasing number of released viruses from the lytic infected cell in the PQ center. This led to a proportional increase in the radius of the PQs, in the range of 300, 400 and 500 µm for 50,000, 100,000, and 200,000 particles, respectively. This indicated that a value of 100,000 to 200,000 released viruses per lysed cell fits best with the experimental data (compare Fig. 8B and E). This conclusion was further supported by the notion that the growth of simulated PQ was similar to the growth of experimental PQs (Fig. 8F). We concluded that the RDF-based intensity profile is a sensitive tool to quantify the effective radius of PQs. Moreover, the number of released particles per lysed cell has an important impact on the spread of HAdVs, and approximately the number of about 100,000 particles released from infected cells match well with the experimental dynamics of our system.

Discussion

The mode of virus transmission contributes to disease progression and pathogenesis, but it is not easy to determine if a virus is transmitted in cell-free or cell-associated manner, since both modes can involve extracellular viruses. In this study we used plaque assays for a computational model describing adenovirus spread between cells. Plaque assays are a classical method to determine viral titers (27). The processes occurring during plaque formation or virus spreading are complex, and variable between different viruses. For example, the spread of enveloped viruses may occur as a result of mixed processes of cell-free and cell-to-cell transmissions (83). Our work here shows that diffusion has a key role in cell-free transmission of species C HAdV-2. Employing TIRF microscopy and virus tracking we directly measured the diffusion constant of HAdV. By incorporating this measurement in a model for cell-free virus transmission, we show that an invariable diffusion constant of HAdV is sufficient to largely describe the spreading of virus in the course of plaque formation in monolayers.

Our study shows that HAdV-2/5 spreads from infected to non-infected cells in a monolayer predominantly by the cell-free mode. We base this conclusion on

several lines of experimental evidence. First, HAdV spread occurred only if the infected donor cell underwent lysis. Second, viral spreading was strongly affected by convection. We show by time-lapse epi-fluorescent microscopy that convection is largely attenuated on cells overlaid with semi-solid agarose medium. Significantly, the plaques in tilted plates formed underneath semi-solid medium had a round appearance. Third, extracellular antibodies largely neutralized adenovirus spreading.

From these findings, we established a computational model for the propagation of HAdV infection in cultured cells. It is a hybrid, discrete and spatio-temporal model with two random components, the time from cell infection to lysis, and the number of progeny viruses released upon lysis. A uniform distribution for the former is justified, since the mechanism of lysis is not known, and for the latter we found a value of 100,000 viruses per cell to best fit the experimental data. Our multi-scale model combines a CA and a partial differential equation, which was discretized to describe the diffusion of viruses in the cell-free environment using the PSE (25). PSE is a powerful method, as shown previously for simulations of biological diffusion processes (85, 87). To our knowledge, the model presented here is the first CA-PSE hybrid model. The model demonstrates good predictive abilities for both qualitative and quantitative phenotypic features of viral spreading, although it does not take into account the movements of cells, and involves simple hexagonal grid geometry (76). The model quantitatively describes that HAdV spreads by diffusion, and under some conditions advection components.

We anticipate that passive mass transfer processes control the progression of infection in confined environments, particularly prone to bulk motions, such as the extracellular fluid in epithelial tissues. As shown here, bulk motions affect the local concentrations of virus particles around uninfected cells, and influence the probability of infection, as documented by hyper-infection. This suggests that high multiplicity infections may have pathological relevance. Additionally, cell-free viral transmissions drive lytic infections with large burst sizes enabling infections of neighboring cells by avidity binding to low affinity receptors, for example, binding of oncolytic species B1 HAdV to CD46 (105). Large burst sizes can also

compensate for genetic deficiencies of individual particles by trans-complementation.

The modelling platform established here provides a basis for analysing cell-free aspects of both lytic and non-lytic viral transmissions. Cell-free lytic transmissions widely occur for both enveloped and non-enveloped viruses. Examples for the former are poxviruses or measles virus, and the latter picornaviruses, reoviruses or adenoviruses (3, 95). Cell-free transmissions neither require particular cell-cell contact sites, nor the down-regulation of viral receptors from infected cells to detach viruses from the producer cell. Cell-free transmissions are also a major pathway for viral spread between individuals through body fluids or organ transplantations. This is also important for viruses, which use intra-organismic cell-cell transmission routes, such as HIV, HCV or herpes viruses (reviewed in 72, 83). In addition, viral spreading by cell lysis is crucial for the therapeutic efficacy of oncolytic viruses, including HAdV (5, 80, 84).

We expect that our model will be useful to analyse cell-free virus transmissions in different disease processes, where it is difficult to experimentally determine the specific impact of cell-free or cell-cell transmission modes. For this, the diffusive properties of most current known viruses can be accurately predicted using the Einstein-Stokes equation, and the CA component of the hybrid model can be readily extended to include proximity effects, which will allow the modelling of cell-cell spreading.

Our model for the passive mass transfer of cell free viruses can potentially be combined with models for cell-to-cell spread, such as a stochastic model described for Sendaivirus spread (21). Combining discrete and random modeling in lytic and non-lytic transmissions can be interesting for enveloped viruses. For example, extracellular enveloped vaccinia viruses use a cell-cell transmission mode to enhance spreading beyond the speed of a single replication cycle (26, 88), whereas intracellular viruses and inclusion particles of aggregated viruses are released upon cell lysis (95). Likewise, the impact of cell-free transmission on human cytomegalovirus (HCMV) or hepatitis virus C (HCV) infections are unknown. It is remarkable, however, that HCMV from endothelial cells is transmitted between endothelial cells by cell-cell contacts and avoids the cell-free

route, whereas HCMV from fibroblasts chooses a cell-free route to infect fibroblasts or endothelial cells (90). Extracellular HCMVs are prevalent, since hyper-immune globulins against HCMV exhibit strong neutralization effects in decidual organ cultures (110). Similarly, antibodies against the hyper-variable region 1 or the CD81 binding site of the HCV E2 glycoprotein have virus-neutralizing effects in co-cultures of producer and acceptor cells, although these effects vary between genotypes suggesting that also virus specific factors contribute the transmission mode (13). For HCMV, it has been shown that the transmission depends on the protein composition of the viruses (90). In addition, the physiology of the tissue plays a major role for the transmission mode. The tight cell-cell contacts in the liver, for example, may favor cell-cell transmission routes of HCV (62), whereas tissues with looser cell-cell contacts may enable viral spread by diffusion (41, 94).

For therapeutic purposes, this opens the possibility of experimentally degrading parts of the extracellular matrix or triggering apoptosis in tumour tissues in order to enhance viral spreading within the tumour by diffusive processes (94). Furthermore, inflammatory conditions with rapidly changing compositions of the extracellular matrix, for example in periodontitis (93), may enhance viral susceptibility by diffusive spreading processes. Our work here lays a foundation for the elucidation of viral cell transmission mechanisms that are determined by parameters, which are difficult to measure in tissues, such as diffusive properties of viruses in extracellular matrix of connective tissue, airway mucus, intestines or cervico-vaginal tracts (42, 53, 67).

Acknowledgments

The authors thank Julia Reinert for help on confirming anti-serum activity, Jo Helmuth for discussion, Martin Engelke for support with TIRF microscopy, Bettina Cardel for cell culture, I-Hsuan Wang for materials supply for the experiments with fluorescently labeled HAdV, and other current and former members of the Greber and Sbalzarini groups for discussions and support. We thank Anja Ehrhardt (Ludwig Maximilians University of Munich, Germany) for the generous gift of

neutralizing anti-Ad5 antiserum. We also thank the following members of the MOSAIC Group, ETH Zurich: Janick Cardinale for his help with measuring RDFs from images, and Omar Awile, Christian Müller, and Rajesh Ramaswamy for their help with the PSE simulation code. This work was supported by a grant from the Swiss National Science Foundation (ProDoc PDFMP3_124927 to UFG), the Swiss SystemsX.ch initiative (grant InfectX to UFG and grant LipidX to UFG and IFS), and the Kanton Zürich (UFG).

References

1. **Ahmed, R., and A. F. Graham.** 1977. Persistent infections in L cells with temperature-sensitive mutants of reovirus. Journal of Virology **23:**250-262.

2. **Amstutz, B., M. Gastaldelli, S. Kälin, N. Imelli, K. Boucke, E. Wandeler, J. Mercer, S. Hemmi, and U. F. Greber.** 2008. Subversion of CtBP1 controlled macropinocytosis by human Adenovirus serotype 3. EMBO J. **27:**956-966.

3. **Bais, S., E. Bartee, M. M. Rahman, G. McFadden, and C. R. Cogle.** 2012. Oncolytic virotherapy for hematological malignancies. Adv Virol **2012:**186512.

4. **Bankhead, A., E. Mancinia, A. Simsc, R. Baric, S. McWeeneyb, and P. Sloot.** 2011. A simulation framework to investigate in vitro viral infection dynamics. Journal of Computational Science **10.1016/j.jocs.2011.08.007**.

5. **Barton, K. N., D. Paielli, Y. Zhang, S. Koul, S. L. Brown, M. Lu, J. Seely, J. Ho Kim, and S. O. Freytag.** 2006. Second-Generation Replication-Competent Oncolytic Adenovirus Armed with Improved Suicide Genes and ADP Gene Demonstrates Greater Efficacy without Increased Toxicity. Mol Ther **13:**347-356.

6. **Beauchemin, C., J. Samuel, and J. Tuszynski.** 2005. A simple cellular automaton model for influenza A viral infections. Journal of theoretical biology **232:**223-234.

7. **Benson, S. D., J. K. Bamford, D. H. Bamford, and R. M. Burnett.** 1999. Viral evolution revealed by bacteriophage PRD1 and human adenovirus coat protein structures. Cell **98:**825-833.

8. **Bergelson, J. M., J. A. Cunningham, G. Droguett, E. A. Kurt-Jones, A. Krithivas, J. S. Hong, M. S. Horwitz, R. L. Crowell, and R. W. Finberg.** 1997. Isolation of a common receptor for Coxsackie B viruses and adenoviruses 2 and 5. Science **275:**1320-1323.

9. **Berk, A. J.** 2007. Adenoviridae: the viruses and their replication, p. 2355-2436. *In* D. M. Knipe and P. M. Howley (ed.), Fields Virology, 5 ed, vol. 2. Lippincott Williams & Wilkins, Philadelphia, PA, USA.

10. **Berk, A. J.** 2005. Recent lessons in gene expression, cell cycle control, and cell biology from adenovirus. Oncogene **24:**7673-7685.

11. **Bocharov, G. A., and A. A. Romanyukha.** 1994. Mathematical Model of Antiviral Immune Response III. Influenza A Vizrus Infection. J. Theor. Biol**:**323-360.

12. **Bremner, K. H., J. Scherer, J. Yi, M. Vershinin, S. P. Gross, and R. B. Vallee.** 2009. Adenovirus transport via direct interaction of cytoplasmic dynein with the viral capsid hexon subunit. Cell Host Microbe **6:**523-535.

13. **Brimacombe, C. L., J. Grove, L. W. Meredith, K. Hu, A. J. Syder, M. V. Flores, J. M. Timpe, S. E. Krieger, T. F. Baumert, T. L. Tellinghuisen, F. Wong-Staal, P. Balfe, and J. A. McKeating.** 2011. Neutralizing antibody-resistant hepatitis C virus cell-to-cell transmission. Journal of Virology **85:**596-605.

14. **Burckhardt, C. J., and U. F. Greber.** 2009. Virus movements on the plasma membrane support infection and transmission between cells. PLoS Pathog **5:**e1000621.

15. **Burckhardt, C. J., M. Suomalainen, P. Schoenenberger, K. Boucke, S. Hemmi, and U. F. Greber.** 2011. Drifting Motions of the Adenovirus Receptor CAR and Immobile Integrins Initiate Virus Uncoating and Membrane Lytic Protein Exposure. Cell Host & Microbe **10:**105-117.

16. **Carpenter, A., T. Jones, M. Lamprecht, C. Clarke, I. Kang, O. Friman, D. Guertin, J. Chang, R. Lindquist, J. Moffat, P. Golland, and D. Sabatini.** 2006. CellProfiler: image analysis software for identifying and quantifying cell phenotypes. Genome Biology **7:**R100.

17. **Charlotte, M., and et al.** 2001. Light deflection and convection in diffusion experiments using holographic interferometry. Journal of Physics D: Applied Physics **34:**3088.

18. **Chen, E. C., S. Yagi, K. R. Kelly, S. P. Mendoza, N. Maninger, A. Rosenthal, A. Spinner, K. L. Bales, D. P. Schnurr, N. W. Lerche, and C. Y. Chiu.** 2011. Cross-species transmission of a novel adenovirus associated with a fulminant pneumonia outbreak in a new world monkey colony. PLoS Pathogens **7:**e1002155.

19. **Chen, P., J. Tian, I. Kovesdi, and J. T. Bruder.** 1998. Interaction of the adenovirus 14.7-kDa protein with FLICE inhibits Fas ligand-induced apoptosis. The Journal of biological chemistry **273:**5815-5820.

20. **Chen, P. H., D. A. Ornelles, and T. Shenk.** 1993. The adenovirus L3 23-kilodalton proteinase cleaves the amino-terminal head domain from cytokeratin 18 and disrupts the cytokeratin network of HeLa cells. J Virol **67:**3507-3514.

21. **Clark, N., K. Tapia, A. Dandapani, B. MacArthur, C. Lopez, and A. Ma'ayan.** 2011. Stochastic model of virus and defective interfering particle spread across mammalian cells with immune response. Cornell University Library **arXiv:1108.4901v1 [q-bio.PE]:**1-22.

22. **Colbere-Garapin, F., C. Christodoulou, R. Crainic, and I. Pelletier.** 1989. Persistent poliovirus infection of human neuroblastoma cells. Proceedings of the National Academy of Sciences of the United States of America **86:**7590-7594.

23. **Davis, D. M., T. Igakura, F. E. McCann, L. M. Carlin, K. Andersson, B. Vanherberghen, A. Sjostrom, C. R. Bangham, and P. Hoglund.** 2003. The protean immune cell synapse: a supramolecular structure with many functions. Seminars in immunology **15:**317-324.

24. **de la Torre, J. C., M. Davila, F. Sobrino, J. Ortin, and E. Domingo.** 1985. Establishment of cell lines persistently infected with foot-and-mouth disease virus. Virology **145:**24-35.

25. **Degond, P., and S. Mas-Gallic.** 1989. The Weighted Particle Method for Convection-Diffusion Equations. Part 1: The Case of an Isotropic Viscosity. Mathematics of Computation **53:**485-507.

26. **Doceul, V., M. Hollinshead, L. van der Linden, and G. L. Smith.** 2010. Repulsion of superinfecting virions: a mechanism for rapid virus spread. Science **327:**873-876.

27. **Dulbecco, R.** 1952. Production of Plaques in Monolayer Tissue Cultures by Single Particles of an Animal Virus. Proceedings of the National Academy of Sciences of the United States of America **38:**747-752.

28. **Einstein, A.** 1905. Über die von der molekularkinetischen Theorie der Wärme geforderte Bewegung von in ruhenden Flüssigkeiten suspendierten Teilchen. Annalen der Physik **322:**549-560.

29. **Engelke, M. F., C. J. Burckhardt, M. K. Morf, and U. F. Greber.** 2011. The Dynactin Complex Enhances the Speed of Microtubule-Dependent Motions of Adenovirus Both Towards and Away from the Nucleus. Viruses **3:**233-253.

30. **Ewers, H., A. E. Smith, I. F. Sbalzarini, H. Lilie, P. Koumoutsakos, and A. Helenius.** 2005. Single-particle tracking of murine polyoma virus-like particles on live cells and artificial membranes. Proc Natl Acad Sci U S A **102:**15110-15115.

31. **Fallaux, F. J., O. Kranenburg, S. J. Cramer, A. Houweling, H. Van Ormondt, R. C. Hoeben, and A. J. Van Der Eb.** 1996. Characterization of 911: a new helper cell line for the titration and propagation of early region 1-deleted adenoviral vectors. Hum Gene Ther **7:**215-222.

32. **Gaggar, A., D. M. Shayakhmetov, and A. Lieber.** 2003. CD46 is a cellular receptor for group B adenoviruses. Nat Med **9:**1408-1412.

33. **Garnett, C. T., D. Erdman, W. Xu, and L. R. Gooding.** 2002. Prevalence and quantitation of species C adenovirus DNA in human mucosal lymphocytes. Journal of Virology **76:**10608-10616.

34. **Gastaldelli, M., N. Imelli, K. Boucke, B. Amstutz, O. Meier, and U. F. Greber.** 2008. Infectious adenovirus type 2 transport through early but not late endosomes. Traffic **9:**2265-2278.

35. **Gazzola, M., C. J. Burckhardt, B. Bayati, M. Engelke, U. F. Greber, and P. Koumoutsakos.** 2009. A stochastic model for microtubule motors describes the in vivo cytoplasmic transport of human adenovirus. PLoS Comp Biol **5:**e1000623.

36. **Gooding, L. R., L. W. Elmore, A. E. Tollefson, H. A. Brady, and W. S. Wold.** 1988. A 14,700 MW protein from the E3 region of adenovirus inhibits cytolysis by tumor necrosis factor. Cell **53:**341-346.

37. **Greber, U. F., and M. Way.** 2006. A super highway to virus infection. Cell **124(4):**741-754.

38. **Greber, U. F., P. Webster, J. Weber, and A. Helenius.** 1996. The role of the adenovirus protease on virus entry into cells. Embo J **15:**1766-1777.

39. **Greber, U. F., M. Willetts, P. Webster, and A. Helenius.** 1993. Stepwise dismantling of adenovirus 2 during entry into cells. Cell **75:**477-486.

40. **Green, M.** 1962. Studies on the biosynthesis of viral DNA. Cold Spring Harbor Symposia on Quantitative Biology **27:**219-235.

41. **Guedan, S., J. J. Rojas, A. Gros, E. Mercade, M. Cascallo, and R. Alemany.** 2010. Hyaluronidase expression by an oncolytic adenovirus enhances its intratumoral spread and suppresses tumor growth. Molecular therapy : the journal of the American Society of Gene Therapy **18:**1275-1283.

42. **Halliday, N. L., and J. J. Tomasek.** 1995. Mechanical Properties of the Extracellular Matrix Influence Fibronectin Fibril Assembly in Vitro. Experimental Cell Research **217:**109-117.

43. **Hausl, M., W. Zhang, N. Muther, C. Rauschhuber, H. Franck, E. Merricks, T. Nichols, M. Kay, and A. Ehrhardt.** 2010. Hyperactive Sleeping Beauty Transposase Enables Persistent Phenotypic Correction in Mice and a Canine Model for Hemophilia B. Mol Ther **18:**1896-1906.

44. **Hayashi, S., and J. C. Hogg.** 2007. Adenovirus infections and lung disease. Curr Opin Pharmacol **7:**237-243.

45. **Helmuth, J. A., C. J. Burckhardt, U. F. Greber, and I. F. Sbalzarini.** 2009. Shape reconstruction of subcellular structures from live cell fluorescence microscopy images. J Struct Biol **167:**1-10.

46. **Hilgendorf, A., J. Lindberg, Z. Ruzsics, S. Honing, A. Elsing, M. Lofqvist, H. Engelmann, and H. G. Burgert.** 2003. Two distinct transport motifs in the adenovirus E3/10.4-14.5 proteins act in concert to down-modulate apoptosis receptors and the epidermal growth factor receptor. J Biol Chem **278:**51872-51884.

47. **Hockney, R. W., and J. W. Eastwood.** 1989. Computer Simulation Using Particles. Taylor & Francis.

48. **Imelli, N., Z. Ruzsics, D. Puntener, M. Gastaldelli, and U. F. Greber.** 2009. Genetic reconstitution of the human adenovirus type 2 temperature-sensitive 1 mutant defective in endosomal escape. Virol J **6:**174.

49. **Incropera, F. P., and D. P. DeWitt.** 1990. Fundamentals of Heat and Mass Transfer, 3rd ed. John Wiley & Sons, New York.

50. **Karim, M. F. A., A. I. M. Ismail, and H. B. Ching.** 2009. Cellular automata modelling of hantarvirus infection. Chaos, Solitons & Fractals **41:**2847-2853.

51. **Komarova, N. L.** 2007. Viral reproductive strategies: How can lytic viruses be evolutionarily competitive? Journal of theoretical biology **249:**766-784.

52. **Krilov, L. R.** 2005. Adenovirus infections in the immunocompromised host. Pediatr Infect Dis J **24:**555-556.

53. **Lai, S. K., Y. Y. Wang, R. Cone, D. Wirtz, and J. Hanes.** 2009. Altering mucus rheology to "solidify" human mucus at the nanoscale. PLoS ONE **4:**e4294.

54. **Leopold, P. L., G. Kreitzer, N. Miyazawa, S. Rempel, K. K. Pfister, E. Rodriguez-Boulan, and R. G. Crystal.** 2000. Dynein- and microtubule-mediated translocation of adenovirus serotype 5 occurs after endosomal lysis. Hum Gene Ther **11:**151-165.

55. **Lewis, P. F., M. A. Schmidt, X. Lu, D. D. Erdman, M. Campbell, A. Thomas, P. R. Cieslak, L. D. Grenz, L. Tsaknardis, C. Gleaves, B. Kendall, and D. Gilbert.** 2009. A community-based outbreak of severe respiratory illness caused by human adenovirus serotype 14. J Infect Dis **199:**1427-1434.

56. **Li, T., S. Kheifets, D. Medellin, and M. Raizen.** 2010. Measurement of the Instantaneous Velocity of a Brownian Particle. Science **328:**1673-1675.

57. **Liang, M.** 2011. Clinical Development of Oncolytic viruses in China. Curr Pharm Biotechnol.

58. **Lichtenstein, D. L., K. Toth, K. Doronin, A. E. Tollefson, and W. S. Wold.** 2004. Functions and mechanisms of action of the adenovirus E3 proteins. Int Rev Immunol **23:**75-111.

59. **Lichtenstein, D. L., and W. S. Wold.** 2004. Experimental infections of humans with wild-type adenoviruses and with replication-competent adenovirus vectors: replication, safety, and transmission. Cancer Gene Ther **11:**819-829.

60. **Lindert, S., M. Silvestry, T. M. Mullen, G. R. Nemerow, and P. L. Stewart.** 2009. Cryo-electron microscopy structure of an adenovirus-integrin complex indicates conformational changes in both penton base and integrin. J Virol **83:**11491-11501.

61. **Liu, H., L. Jin, S. B. Koh, I. Atanasov, S. Schein, L. Wu, and Z. H. Zhou.** 2010. Atomic structure of human adenovirus by cryo-EM reveals interactions among protein networks. Science **329:**1038-1043.

62. **Loo, Y. M., D. M. Owen, K. Li, A. K. Erickson, C. L. Johnson, P. M. Fish, D. S. Carney, T. Wang, H. Ishida, M. Yoneyama, T. Fujita, T. Saito, W. M. Lee, C. H. Hagedorn, D. T. Lau, S. A. Weinman, S. M. Lemon, and M. Gale, Jr.** 2006. Viral and therapeutic control of IFN-beta promoter stimulator 1 during hepatitis C virus infection. Proceedings of the National Academy of Sciences of the United States of America **103:**6001-6006.

63. **Lutschg, V., K. Boucke, S. Hemmi, and U. F. Greber.** 2011. Chemotactic anti-viral cytokines promote infectious apical entry of human adenovirus into polarized epithelial cells, p. DOI: 10.1038/ncomms1391, Nat Commun, vol. 2. Nature Publishing Group.

64. **Mallet, D. G., K.-J. Heymer, R. G. Rank, and D. P. Wilson.** 2009. Chlamydial infection and spatial ascension of the female genital tract: a novel hybrid cellular automata and continuum mathematical model. FEMS Immunology & Medical Microbiology **57:**173-182.

65. **Mangel, W. F., M. L. Baniecki, and W. J. McGrath.** 2003. Specific interactions of the adenovirus proteinase with the viral DNA, an 11-amino-acid viral peptide, and the cellular protein actin. Cell Mol Life Sci **60:**2347-2355.

66. **Massanella, M., I. Puigdomenech, C. Cabrera, M. T. Fernandez-Figueras, A. Aucher, G. Gaibelet, D. Hudrisier, E. Garcia, M. Bofill, B. Clotet, and J. Blanco.** 2009. Antigp41 antibodies fail to block early events of virological synapses but inhibit HIV spread between T cells. AIDS **23:**183-188.

67. **Matsui, H., V. E. Wagner, D. B. Hill, U. E. Schwab, T. D. Rogers, B. Button, R. M. Taylor, R. Superfine, M. Rubinstein, B. H. Iglewski, and R. C. Boucher.** 2006. A physical linkage between cystic fibrosis airway surface dehydration and Pseudomonas aeruginosa biofilms. Proceedings of the National Academy of Sciences **103:**18131-18136.

68. **Mazurov, D., A. Ilinskaya, G. Heidecker, P. Lloyd, and D. Derse.** 2010. Quantitative comparison of HTLV-1 and HIV-1 cell-to-cell infection with new replication dependent vectors. PLoS Pathogens **6:**e1000788.

69. **McGavern, D. B., and S. S. Kang.** 2011. Illuminating viral infections in the nervous system. Nature reviews. Immunology **11:**318-329.

70. **Meier, O., and U. F. Greber.** 2003. Adenovirus endocytosis. J Gene Med **5:**451-462.

71. **Metzgar, D., M. Osuna, A. E. Kajon, A. W. Hawksworth, M. Irvine, and K. L. Russell.** 2007. Abrupt emergence of diverse species B adenoviruses at US military recruit training centers. J Infect Dis **196:**1465-1473.

72. **Mothes, W., N. M. Sherer, J. Jin, and P. Zhong.** 2010. Virus cell-to-cell transmission. J Virol **84:**8360-8368.

73. **Munoz, F. M., P. A. Piedra, and G. J. Demmler.** 1998. Disseminated adenovirus disease in immunocompromised and immunocompetent children. Clinical infectious diseases : an official publication of the Infectious Diseases Society of America **27:**1194-1200.

74. **Nakano, M. Y., and U. F. Greber.** 2000. Quantitative microscopy of fluorescent adenovirus entry. J. Struct. Biol. **129:**57-68.

75. **Nilsson, E. C., R. J. Storm, J. Bauer, S. M. Johansson, A. Lookene, J. Angstrom, M. Hedenstrom, T. L. Eriksson, L. Frangsmyr, S. Rinaldi, H. J. Willison, F. Pedrosa Domellof, T. Stehle, and N. Arnberg.** 2011. The GD1a glycan is a cellular receptor for adenoviruses causing epidemic keratoconjunctivitis. Nature Medicine **17:**105-109.

76. **Othmer, H. G., and L. E. Scriven.** 1971. Instability and dynamic pattern in cellular networks. Journal of Theoretical Biology **32:**507-537.

77. **Parks, W. P., J. L. Melnick, R. Rongey, and H. D. Mayor.** 1967. Physical assay and growth cycle studies of a defective adeno-satellite virus. Journal of Virology **1:**171-180.

78. **Pearson, J. E., P. Krapivsky, and A. S. Perelson.** 2011. Stochastic theory of early viral infection: continuous versus burst production of virions. PLoS computational biology **7:**e1001058.

79. **Perelson, A. S.** 2002. Modelling viral and immune system dynamics. Nature reviews. Immunology **2:**28-36.

80. **Pesonen, S., L. Kangasniemi, and A. Hemminki.** 2010. Oncolytic adenoviruses for the treatment of human cancer: focus on translational and clinical data. Molecular Pharmaceutics**:**null-null.

81. **Puntener, D., M. F. Engelke, Z. Ruzsics, S. Strunze, C. Wilhelm, and U. F. Greber.** 2011. Stepwise loss of fluorescent core protein V from human adenovirus during entry into cells. J Virol **85:**481-496.

82. **Reddy, V. S., S. K. Natchiar, P. L. Stewart, and G. R. Nemerow.** 2010. Crystal structure of human adenovirus at 3.5 A resolution. Science **329:**1071-1075.

83. **Sattentau, Q.** 2008. Avoiding the void: cell-to-cell spread of human viruses. Nature reviews. Microbiology **6:**815-826.

84. **Sauthoff, H., J. Hu, C. Maca, M. Goldman, S. Heitner, H. Yee, T. Pipiya, W. N. Rom, and J. G. Hay.** 2003. Intratumoral spread of wild-type adenovirus is limited after local injection of human xenograft tumors: virus persists and spreads systemically at late time points. Hum Gene Ther **14:**425-433.

85. **Sbalzarini, I. F., A. Hayer, A. Helenius, and P. Koumoutsakos.** 2006. Simulations of (an)isotropic diffusion on curved biological surfaces. Biophys J **90:**878-885.

86. **Sbalzarini, I. F., and P. Koumoutsakos.** 2005. Feature point tracking and trajectory analysis for video imaging in cell biology. J Struct Biol **151:**182-195.

87. **Sbalzarini, I. F., A. Mezzacasa, A. Helenius, and P. Koumoutsakos.** 2005. Effects of organelle shape on fluorescence recovery after photobleaching. Biophys J **89:**1482-1492.

88. **Scaplehorn, N., A. Holmstrom, V. Moreau, F. Frischknecht, I. Reckmann, and M. Way.** 2002. Grb2 and Nck act cooperatively to promote actin-based motility of vaccinia virus. Curr Biol **12:**740-745.

89. **Schmitz, H., R. Wigand, and W. Heinrich.** 1983. Worldwide epidemiology of human adenovirus infections. Am J Epidemiol **117:**455-466.

90. **Scrivano, L., C. Sinzger, H. Nitschko, U. H. Koszinowski, and B. Adler.** 2011. HCMV spread and cell tropism are determined by distinct virus populations. PLoS Pathogens **7:**e1001256.

91. **Sigal, A., J. T. Kim, A. B. Balazs, E. Dekel, A. Mayo, R. Milo, and D. Baltimore.** 2011. Cell-to-cell spread of HIV permits ongoing replication despite antiretroviral therapy. Nature.

92. **Sirena, D., B. Lilienfeld, M. Eisenhut, S. Kaelin, K. Boucke, R. R. Beerli, L. Vogt, C. Ruedl, M. F. Bachmann, U. F. Greber, and S. Hemmi.** 2004. The human membrane cofactor CD46 is a receptor for species B Adenovirus serotype 3. J. Virol. **78:**4454-4462.

93. **Slots, J.** 2010. Human viruses in periodontitis. Periodontol 2000 **53:**89-110.

94. **Smith, E., J. Breznik, and B. D. Lichty.** 2011. Strategies to enhance viral penetration of solid tumors. Human gene therapy **22:**1053-1060.

95. **Smith, G. L., and M. Law.** 2004. The exit of vaccinia virus from infected cells. Virus research **106:**189-197.

96. **Spector, D., and R. Goldman.** 2006. Basic methods in microscopy. Protocols and concepts from cells: a laboratory manual. Cold Spring Habor Press, Cold Spring Habor.

97. **Stafford, M. A., L. Corey, Y. Cao, E. S. Daar, D. D. Ho, and A. S. Perelson.** 2000. Modeling Plasma Virus Concentration during Primary HIV Infection. Journal of Theoretical Biology **203:**285-301.

98. **Strunze, S., M. F. Engelke, I.-H. Wang, D. Puntener, K. Boucke, S. Schleich, M. Way, P. Schoenenberger, C. J. Burckhardt, and U. F. Greber.** 2011. Kinesin-1-mediated capsid disassembly and disruption of the nuclear pore complex promote virus infection. Cell Host & Microbe **10:**210-223.

99. **Suomalainen, M., M. Y. Nakano, K. Boucke, S. Keller, R. P. Stidwill, and U. F. Greber.** 1999. Microtubule-dependent minus and plus end-directed motilities are competing processes for nuclear targeting of adenovirus. J. Cell Biol. **144:**657-672.

100. **Tam, P. E., and R. P. Messner.** 1999. Molecular mechanisms of coxsackievirus persistence in chronic inflammatory myopathy: viral RNA

persists through formation of a double-stranded complex without associated genomic mutations or evolution. Journal of Virology **73:**10113-10121.

101. **Tang, Q., U. Lundholm-Beauchamp, and H. S. Ginsberg.** 1997. Spontaneous occurrence of early region 1A reiteration mutants of type 5 adenovirus in persistently infected human T-lymphocytes. Virology **230:**281-291.

102. **Tollefson, A. E., A. Scaria, T. W. Hermiston, J. S. Ryerse, L. J. Wold, and W. S. Wold.** 1996. The adenovirus death protein (E3-11.6K) is required at very late stages of infection for efficient cell lysis and release of adenovirus from infected cells. J Virol **70:**2296-2306.

103. **Tollefson, A. E., A. Scaria, S. K. Saha, and W. S. Wold.** 1992. The 11,600-MW protein encoded by region E3 of adenovirus is expressed early but is greatly amplified at late stages of infection. Journal of Virology **66:**3633-3642.

104. **Tollefson, A. E., K. Toth, K. Doronin, M. Kuppuswamy, O. A. Doronina, D. L. Lichtenstein, T. W. Hermiston, C. A. Smith, and W. S. M. Wold.** 2001. Inhibition of TRAIL-induced apoptosis and forced internalization of TRAIL receptor 1 by adenovirus proteins. Journal of Virology **75:**8875-8887.

105. **Trinh, H. V., G. Lesage, V. Chennamparampil, B. Vollenweider, C. J. Burckhardt, S. Schauer, M. Havenga, U. F. Greber, and S. Hemmi.** 2012. Avidity binding of human adenovirus serotypes 3 and 7 to the membrane cofactor CD46 triggers infection. Journal of Virology **86:**1623-1637.

106. **Trotman, L. C., N. Mosberger, M. Fornerod, R. P. Stidwill, and U. F. Greber.** 2001. Import of adenovirus DNA involves the nuclear pore complex receptor CAN/Nup214 and histone H1. Nature Cell Biology **3:**1092-1100.

107. **van Oostrum, J., and R. M. Burnett.** 1985. Molecular composition of the adenovirus type 2 virion. J. Virol. **56:**439-448.

108. **Wang, H., Z. Y. Li, Y. Liu, J. Persson, I. Beyer, T. Moller, D. Koyuncu, M. R. Drescher, R. Strauss, X. B. Zhang, J. K. Wahl, 3rd, N. Urban, C. Drescher, A. Hemminki, P. Fender, and A. Lieber.** 2011. Desmoglein 2 is a receptor for adenovirus serotypes 3, 7, 11 and 14. Nature Medicine **17:**96-104.

109. **Warming, S., N. Costantino, D. L. Court, N. A. Jenkins, and N. G. Copeland.** 2005. Simple and highly efficient BAC recombineering using galK selection. Nucleic Acids Research **33:**e36.

110. **Weisblum, Y., A. Panet, Z. Zakay-Rones, R. Haimov-Kochman, D. Goldman-Wohl, I. Ariel, H. Falk, S. Natanson-Yaron, M. D. Goldberg, R. Gilad, N. S. Lurain, C. Greenfield, S. Yagel, and D. G. Wolf.** 2011. Modeling of human cytomegalovirus maternal-fetal transmission in a novel decidual organ culture. Journal of Virology **85:**13204-13213.

111. **Wennier, S., S. Li, and G. McFadden.** 2011. Oncolytic virotherapy for pancreatic cancer. Expert reviews in molecular medicine **13:**e18.

112. **Wiethoff, C. M., H. Wodrich, L. Gerace, and G. R. Nemerow.** 2005. Adenovirus protein VI mediates membrane disruption following capsid disassembly. J Virol **79:**1992-2000.

113. **Wu, W., D. C. Blythe, H. Loyd, R. H. Mealey, R. L. Tallmadge, K. S. Dorman, and S. Carpenter.** 2011. Decreased infectivity of a neutralization-resistant equine infectious anemia virus variant can be overcome by efficient cell-to-cell spread. Journal of Virology.

114. **Zhang, J., and E. I. Shakhnovich.** 2009. Slowly replicating lytic viruses: pseudolysogenic persistence and within-host competition. Physical Review Letters **102:**178103.

115. **Zorzenon dos Santos, R. M., and S. Coutinho.** 2001. Dynamics of HIV Infection: A Cellular Automata Approach. Physical Review Letters **87:**168102-168101_168102-168104.

Figures legends

Fig. 1: The formation of plaques around infected lysed cells

A transgenic, replication-competent Ad2 with the dE3B region substituted by a CMV-GFP cassette (Ad2-dE3B-GFP) was used to infect monolayers of human lung carcinoma A549 (HLC-A549) cells at $5 \bullet 10^{-7}$ mg/ml in 200 µl of culture medium. Infection progression was imaged by multi-site time-lapse fluorescence microscopy. Panel (**A**) shows the GFP signals from infected cells at indicated time points of infection. Note the occurrence of circular zones of GFP-positive cells around an initially infected cell, a so-called plaque. The arrows in the figure points to the lysing infected cell. Panel (**B**) is an overlay of the GFP signal from infected cells (green), Hoechst 33342 nuclear live dye (Hoechst, blue), and propidium iodide for lysed cells (PI, red). See also Fig. S1 and Movie S1.

Fig. 2: Cell-to-cell of infection occurs through the extracellular medium

(**A, B**) Monolayers of HLC-A549 were inoculated with Ad2-dE3B-GFP expressing eGFP. 2h later, the inoculum was substituted with liquid or gel-forming (semi-solid) medium (0.6% of ultra low melting agarose mass). This agarose is liquid at 37°C, gels at room temperature, and remains gelled at 37°C. PQs exhibit comet-like shapes in liquid medium and circular shapes in semi-solid medium. The micrographs are composites of stitched images taken from multiple sites in 96-well plates at 113.5 hpi. (**C**) Neutralizing antiserum against HAdV in the culture medium inhibits viral spreading. HLC-A549 cells grown in monolayers in 96-well plates were inoculated with 0.1 ml of medium containing 10^{-7} mg/ml Ad2-dE3B-GFP for 24 h, supplemented with antiserum containing medium, and then imaged at indicated time points. Scale bar = 1 mm. See also Fig. S2 and Fig. S3, and Movie S2, Movie S3.

Fig. 3: Replication-defective HAdV spreads to neighboring cells from an infected donor cell

Ad2-dE1-GFP infected HER-911 donor cells were seeded at limiting dilutions onto HLC-A549 acceptor cells (1 in 800), which can be infected but do not produce virus particles. The figure shows PQs of Ad2-dE1-GFP, Hoechst and propidium

iodide (PI) composites of a single round of infection. The arrows point to a lysing HER-911 cell. See also Fig. S4 and Fig. S5.

Fig. 4: A hybrid model consisting of a cellular automaton (CA) - particle strength exchange (PSE)

(**A**) Flow chart of the CA-PSE model, and (**B**) cell state flow chart. $N_{viruses}$ is the number of diffusing, cell-free viral particles, p has a random value from a uniform distribution U(0,1), $P(N_{viruses} \mid Infected)$ is the probability of infection upon exposure to $N_{viruses}$ virus particles, dt is the CA time step, P(lysis) is the probability of cell lysis, P_T(death) is the time-dependent probability for an uninfected cell to die, and T_{lysis} is the time until cell lysis.

Fig. 5: Parameters of the hybrid cellular automaton - particle strength exchange (CA-PSE) model

The parameters listed on the left hand side affect the CA while parameters listed on the right hand side affect the PSE. Parameter values were all derived from experiments in this study except the number of viral particles produced from a lytic infected cell. This latter value was adopted from (40).

Fig. 6: Infection probability, GFP expression kinetics and overall cell death are viral dose-dependent

(**A**) Multi-site time-lapse imaging of HLC-A549 cells infected with different amounts. Automated computational cell segmentation using CellProfiler was used to count all cells and determine the fraction of infected cells. This allowed measuring the infection probability as a function of input virus protein concentration. Measurements were performed 72 hpi.

(**B**) To convert the virus protein concentration to the number of viral particles, we used a theoretical number of HAdV particles (TNAP). It was determined from the protein mass of an individual adenovirus particle as described in equation (1). The mean GFP intensity (averaged per well) was measured for each virus concentration. Measurements were made per concentration and per time point with a time resolution of 1 h. This allowed calibrating the GFP intensity increase as a function of time and input Ad2-dE3B-GFP. See also Movie S4 and Fig. S7.

(**C**) Cells were imaged in the presence of propidium iodide dye (PI) and Hoechst 33342 dye (Hoechst) over 120.5 h. The number of PI-positive cells was plotted for infected (blue) and non-infected (red) cells. Quantification was by CellProfiler based on the Hoechst and PI signals.

Fig. 7: Simulation output from the hybrid cellular automaton - particle strength exchange

An example of a simulation for AdV2-dE3B-GFP infection is shown. The figure shows the hexagonal CA cell mesh outlined in blue with color-coded cells: red – dead, green – infected. The green color intensities represent relative GFP levels. See also Supplementary Movie S5.

Fig. 8: Model validation by radial distribution function of PQ reveals how local HAdV concentrations affect infection

(**A**) The micrograph and the fluorescence intensity profile depicted in the line graph represent a PQ from a single round HLC-A549 infection with Ad2-dE1-GFP, analyzed by the radial distribution function (RDF). The RDF provides a distance-dependent sampling of the mean fluorescence intensity averaged around concentric rings around the PQ center. The radius (r) of a PQ is defined as the distance between the PQ center and the radial position where the fluorescence intensity drops to the level of background intensity, which was estimated from cells in uninfected control wells. Panels B-C show average RDFs from 15 different experimental PQs with Ad2-dE3B-GFP (**B**) or simulated PQs (**C**) 113 hpi (solid line), including the +/- one sigma band (dashed lines), and the background fluorescence from the experimental images (dotted line). Fluorescence values were obtained using linear interpolation in the experimental calibration curve. In (**C**), the number of released progeny virus particles was assumed to be 100,000 per lytic infected cell. Hyper-infection of cells close to the lytic infected cell in the PQ center was allowed in the simulation. Panel (**D**) depicts the average simulated RDF without hyper-infection 113 hpi. Panel (**E**) shows the average simulated mean RDFs for different numbers of released progeny viruses per lysed cell 113 hpi, 50,000 particles (green), 100,000 particles (blue), 200,000 particles (red) allowing for hyper-infection. Panel (**F**) shows three representative examples for

time resolved PQ formation from Ad2-dE3B-GFP infected HLC-A549 cells (colored lines), and a simulated PQ using 100,000 released particles per cell and allowing for hyper-infection (dashed grey line). The observation period was from 43 to 113 hpi.

Table 1: Reynolds numbers (Re) for beads with variable size

bead diameter (m)	maximal Re from instantaneous speed*	maximal Re from mean speed*	Re from theoretical instantaneous speed*
$3.98 \cdot 10^{-08}$	-	-	$2.01 \cdot 10^{-2}$
$1.14 \cdot 10^{-07}$	$1.72 \cdot 10^{-4}$	$3.82 \cdot 10^{-5}$	$1.19 \cdot 10^{-2}$
$2.09 \cdot 10^{-07}$	$5.20 \cdot 10^{-4}$	$7.29 \cdot 10^{-5}$	$8.77 \cdot 10^{-3}$
$5.16 \cdot 10^{-07}$	$1.39 \cdot 10^{-3}$	$3.06 \cdot 10^{-4}$	$5.58 \cdot 10^{-3}$
$7.48 \cdot 10^{-07}$	$1.29 \cdot 10^{-3}$	$2.46 \cdot 10^{-4}$	$4.63 \cdot 10^{-3}$
$1.02 \cdot 10^{-06}$	$2.56 \cdot 10^{-3}$	$4.68 \cdot 10^{-4}$	$3.97 \cdot 10^{-3}$

* Material, methods and models for detailed description of calculation methods

Table 2: Phenotypic parameters of biological and *in silico* plaques (PQ)

	mean radius, (µm)*	**infected cells (number)***	**total cells (number)***	**speed of spreading front (µm/h)***
biological PQs	471±58	629±262	1776±418	4±1
in silico PQs	513±55	347±21	1591±334	5.8±0.6

* Materials, methods and models provide details on the calculation methods

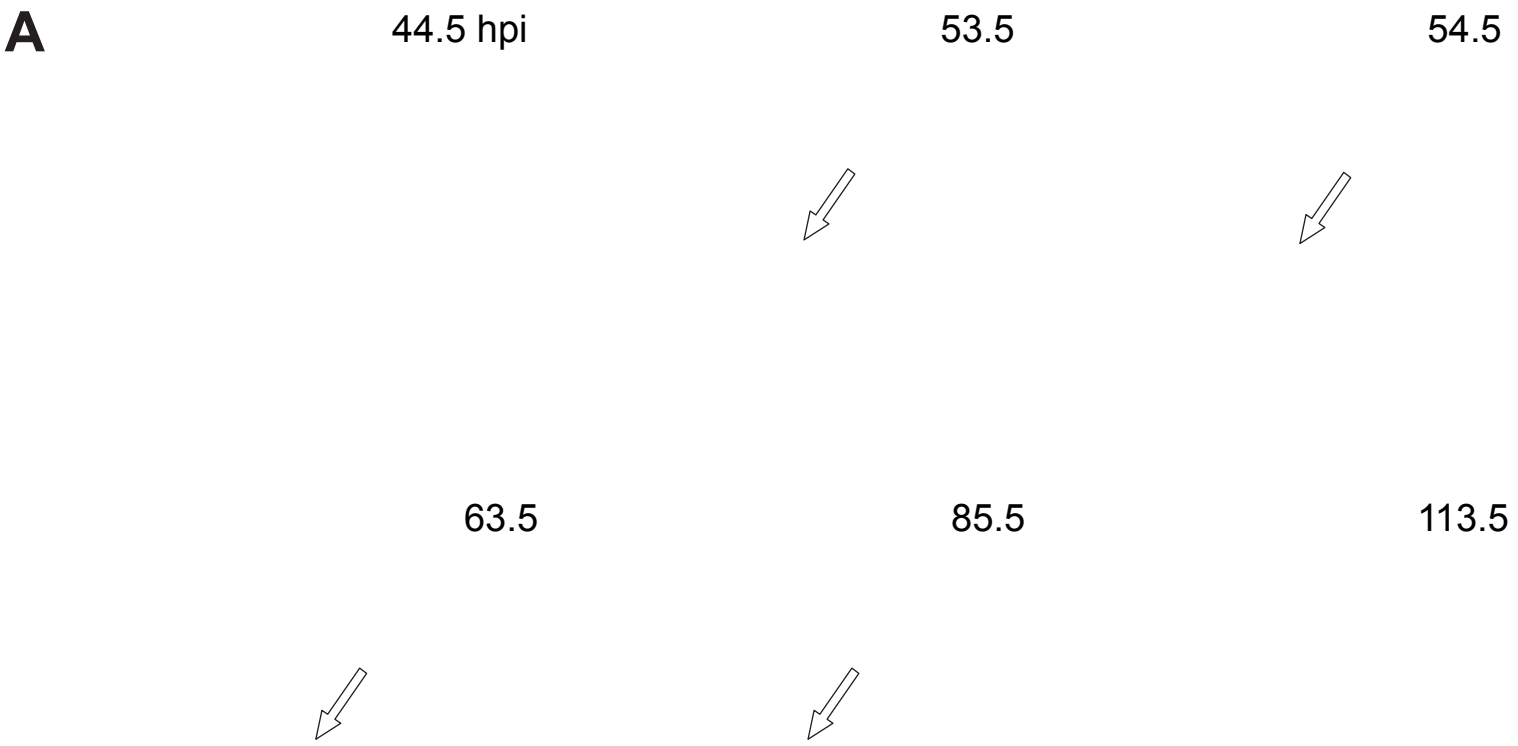
A
44.5 hpi
53.5
54.5
63.5
85.5
113.5

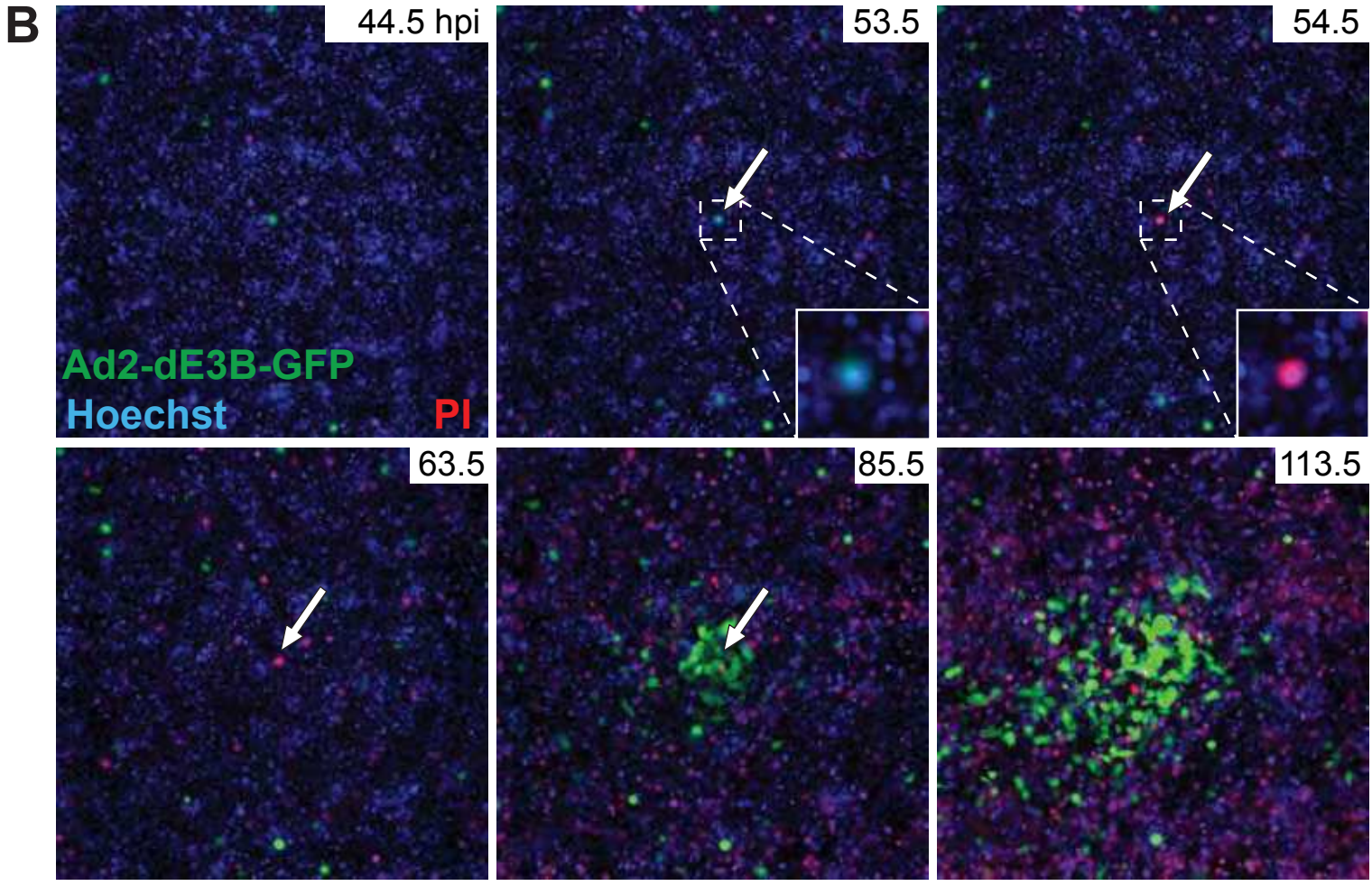
B
44.5 hpi
53.5
54.5
Ad2-dE3B-GFP
Hoechst
PI
63.5
85.5
113.5

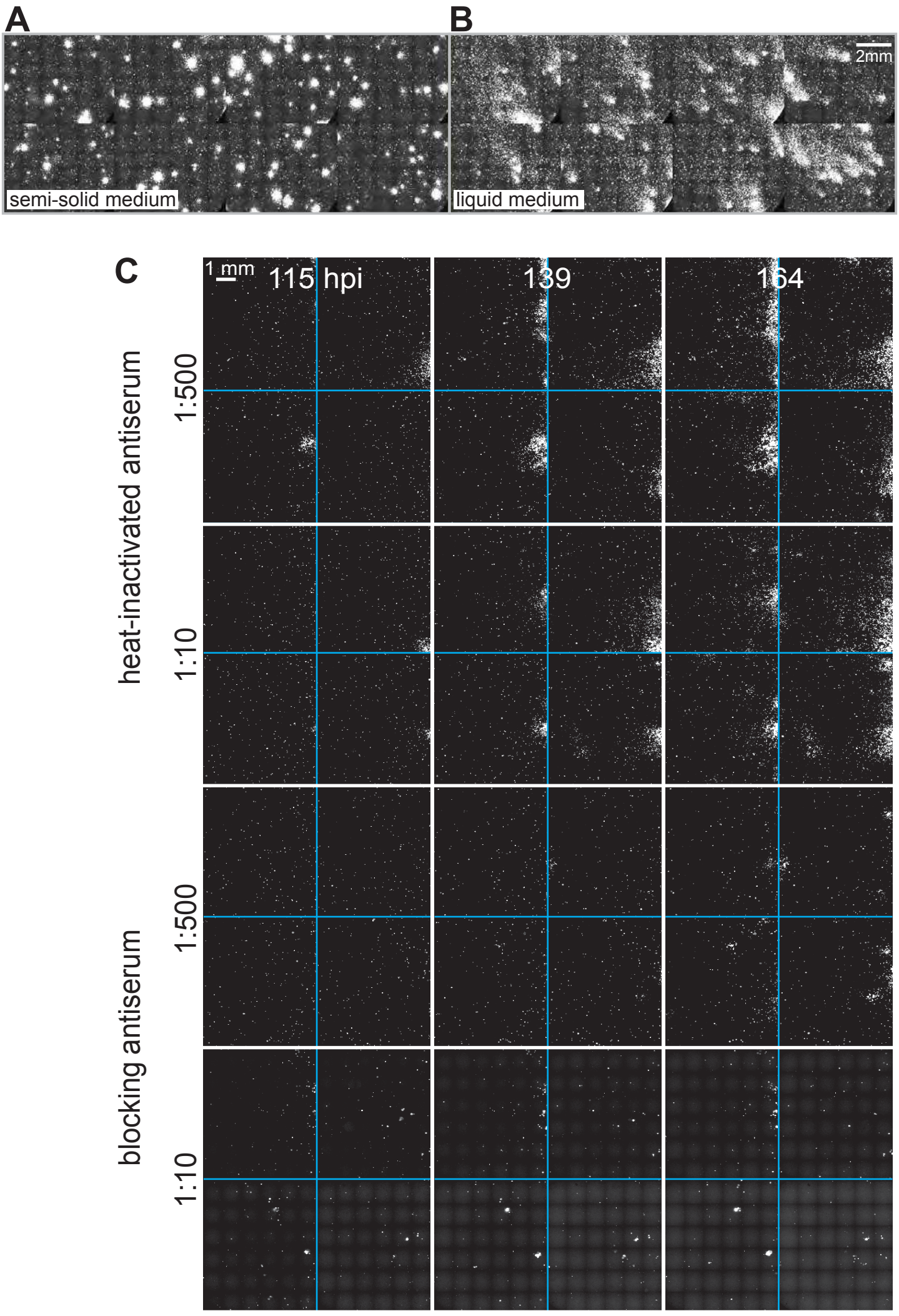
A
B
2mm
semi-solid medium
liquid medium
C
1 mm
115 hpi
139
164
heat-inactivated antiserum
1:500
1:10
blocking antiserum
1:500
1:10

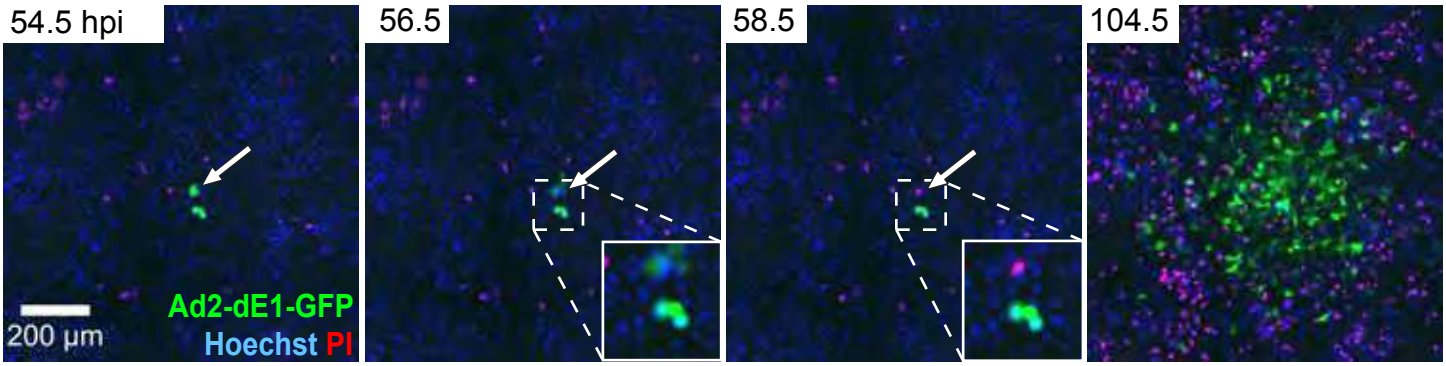
54.5 hpi
56.5
58.5
104.5
200 μm
Ad2-dE1-GFP
Hoechst PI

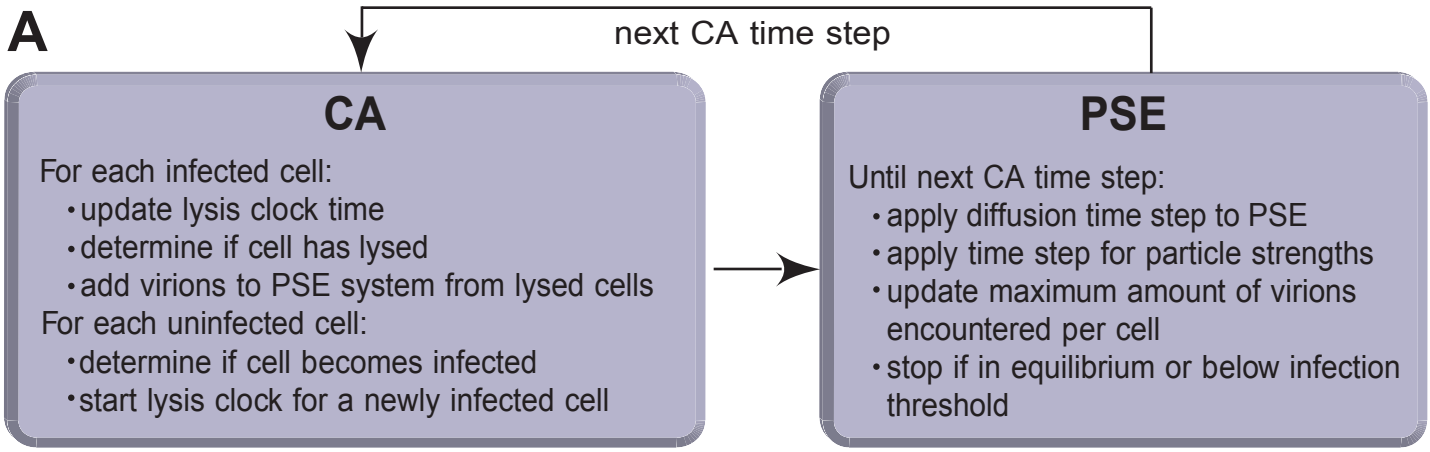
A
next CA time step
CA
For each infected cell:
• update lysis clock time
• determine if cell has lysed
• add virions to PSE system from lysed cells
For each uninfected cell:
• determine if cell becomes infected
• start lysis clock for a newly infected cell
PSE
Until next CA time step:
• apply diffusion time step to PSE
• apply time step for particle strengths
• update maximum amount of virions encountered per cell
• stop if in equilibrium or below infection threshold

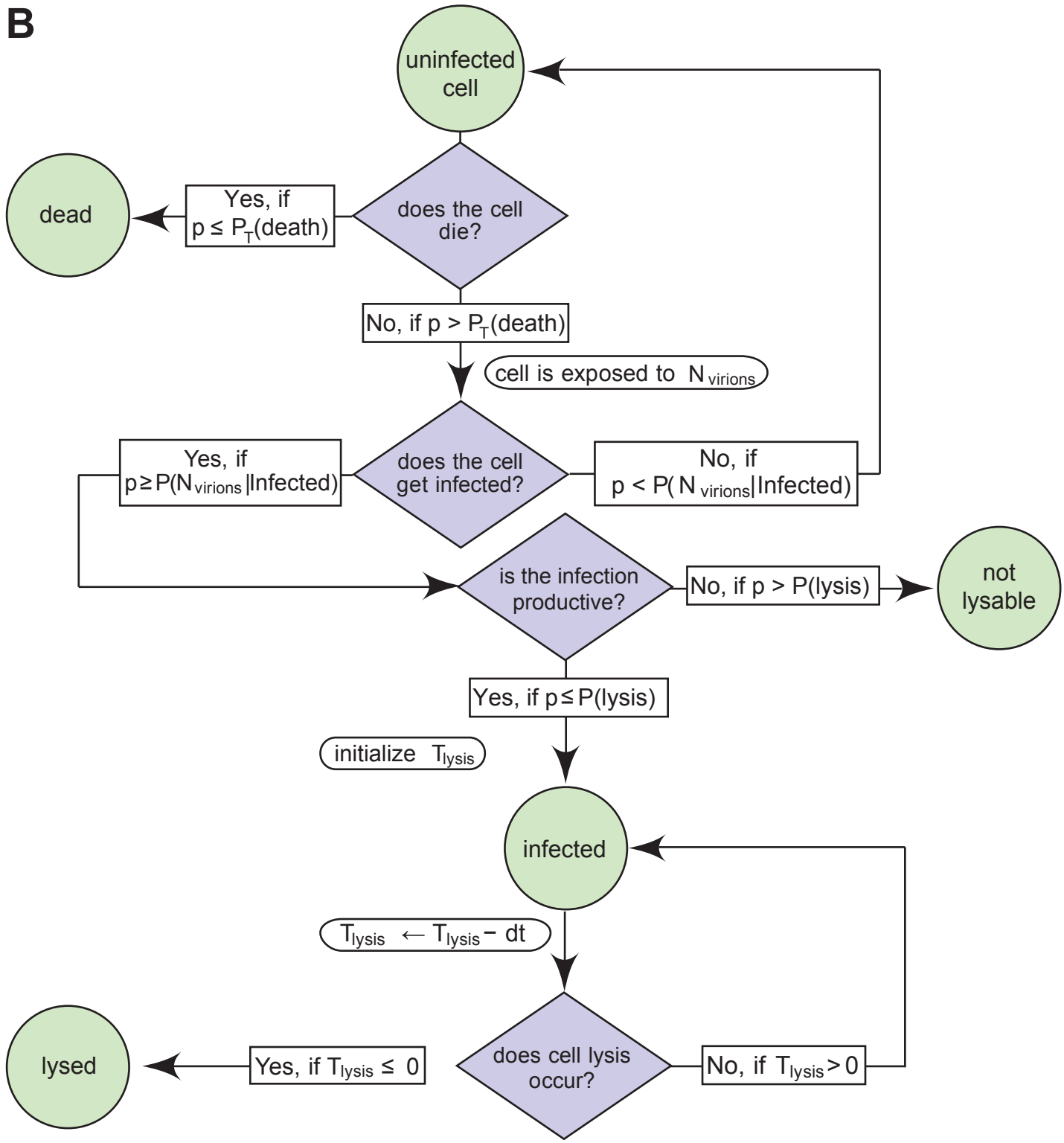
B
uninfected cell
does the cell die?
Yes, if p ≤ P_T(death)
dead
No, if p > P_T(death)
cell is exposed to N virions
does the cell get infected?
Yes, if p ≥ P(N virions | Infected)
No, if p < P(N virions | Infected)
is the infection productive?
No, if p > P(lysis)
not lysable
Yes, if p ≤ P(lysis)
initialize T_lysis
infected
T_lysis ← T_lysis − dt
does cell lysis occur?
No, if T_lysis > 0
Yes, if T_lysis ≤ 0
lysed

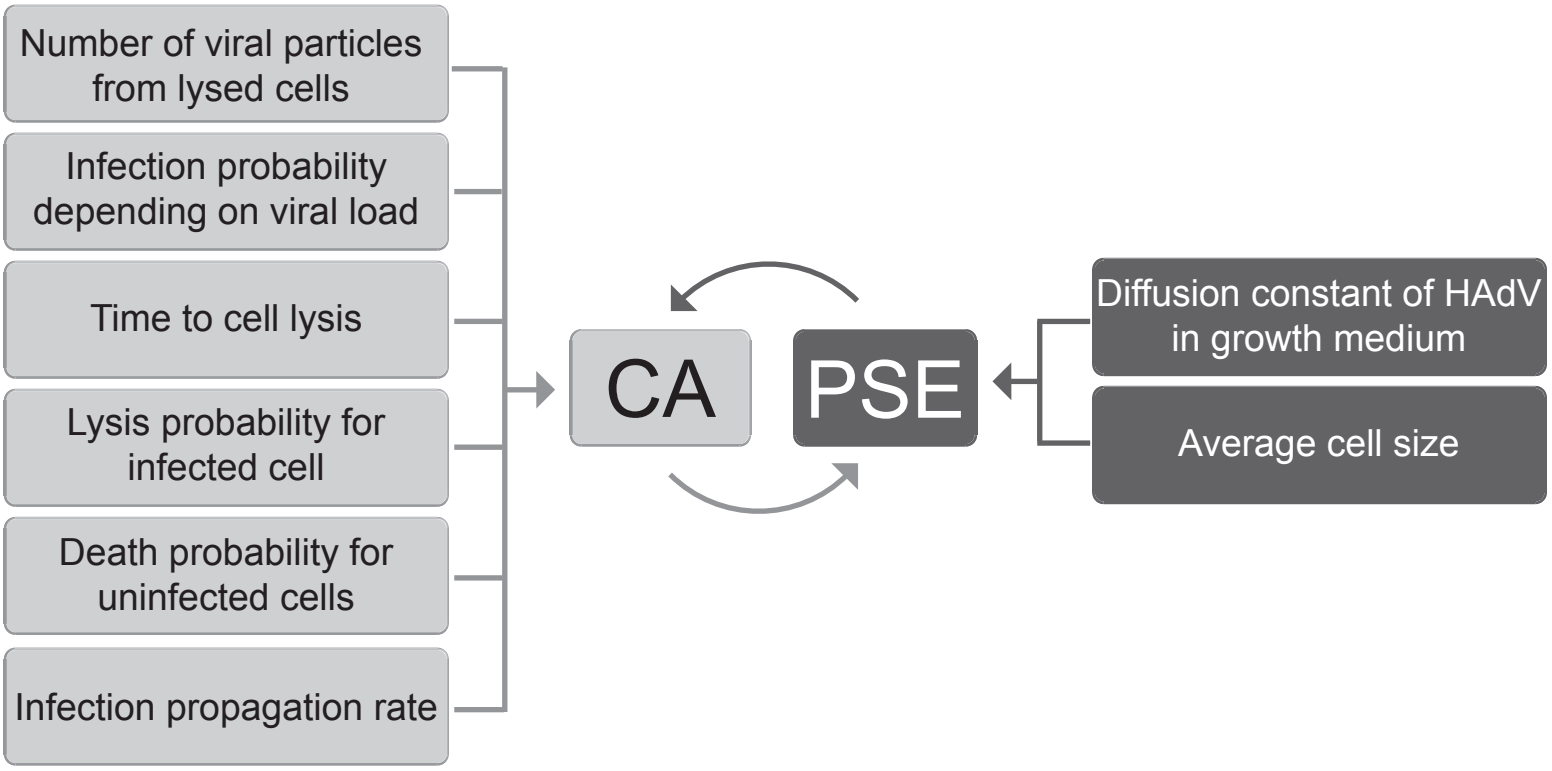
Number of viral particles from lysed cells
Infection probability depending on viral load
Time to cell lysis
Lysis probability for infected cell
Death probability for uninfected cells
Infection propagation rate
CA
PSE
Diffusion constant of HAdV in growth medium
Average cell size

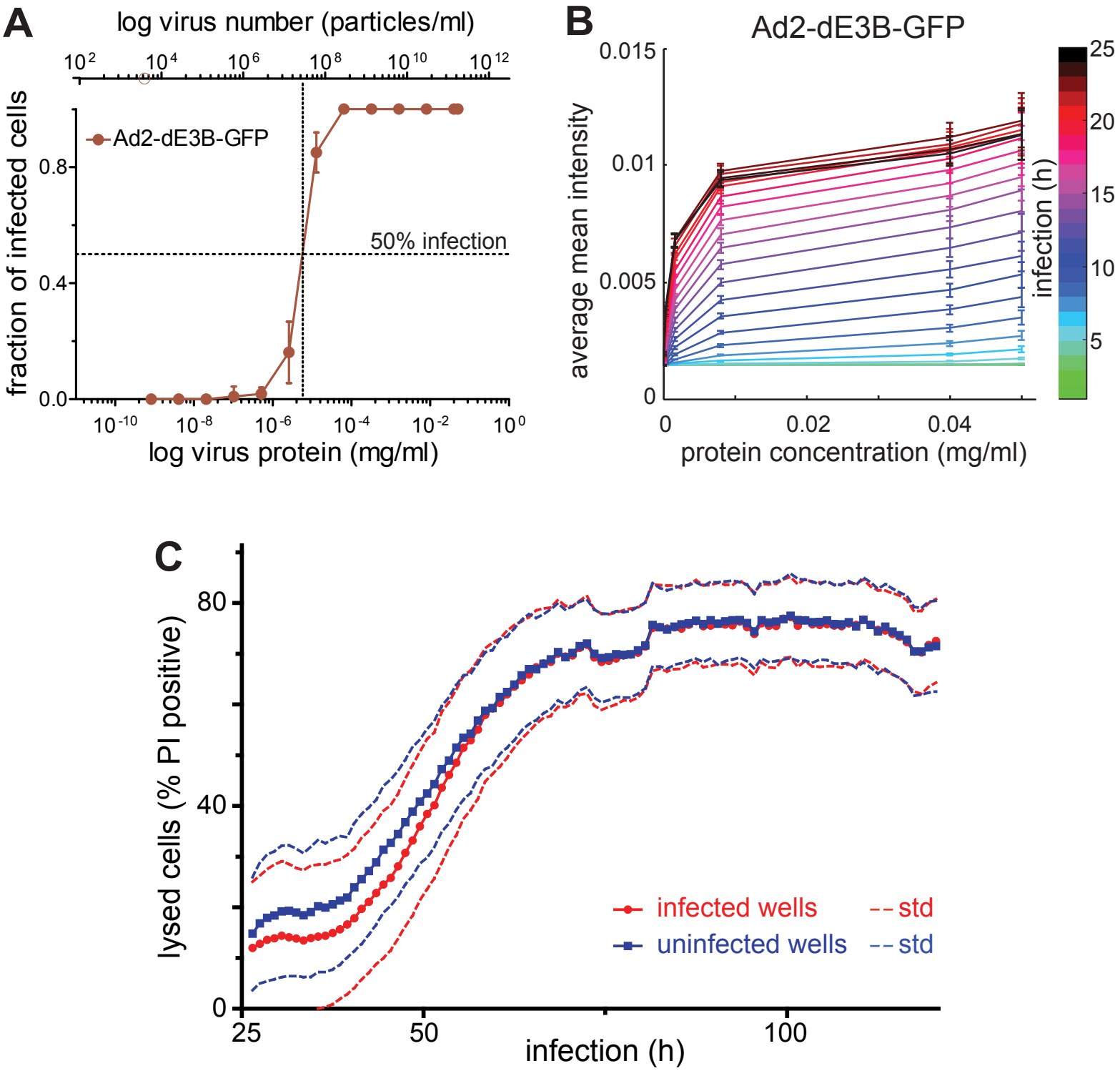
A
log virus number (particles/ml)
10^2 10^4 10^6 10^8 10^{10} 10^{12}
Ad2-dE3B-GFP
50% infection
fraction of infected cells
0.0
0.4
0.8
10^{-10} 10^{-8} 10^{-6} 10^{-4} 10^{-2} 10^0
log virus protein (mg/ml)
B
Ad2-dE3B-GFP
average mean intensity
0
0.005
0.01
0.015
0
0.02
0.04
protein concentration (mg/ml)
infection (h)
5
10
15
20
25
C
lysed cells (% PI positive)
0
40
80
25
50
100
infection (h)
infected wells
std
uninfected wells
std

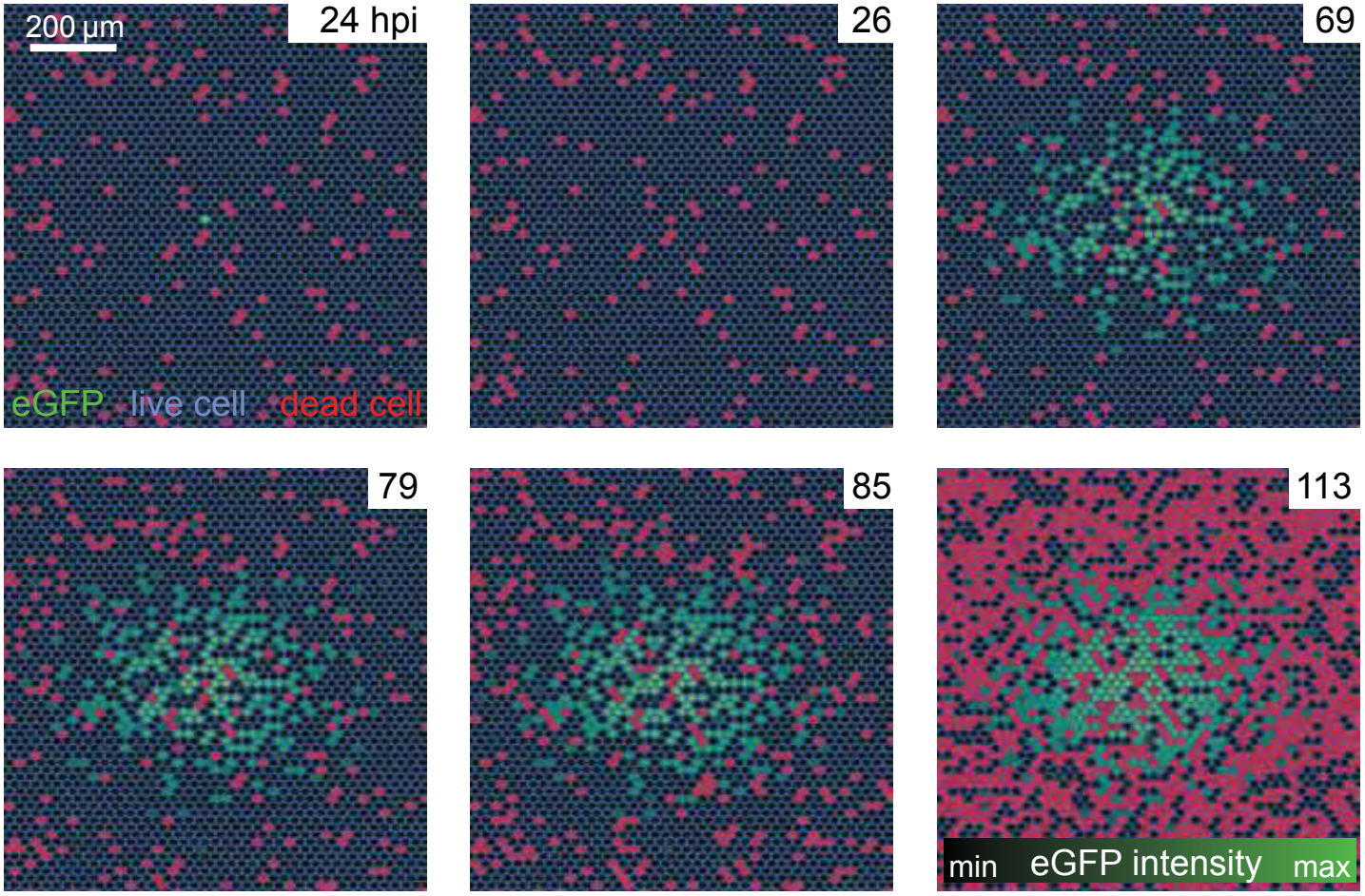
200 µm
24 hpi
26
69
eGFP live cell dead cell
79
85
113
min eGFP intensity max

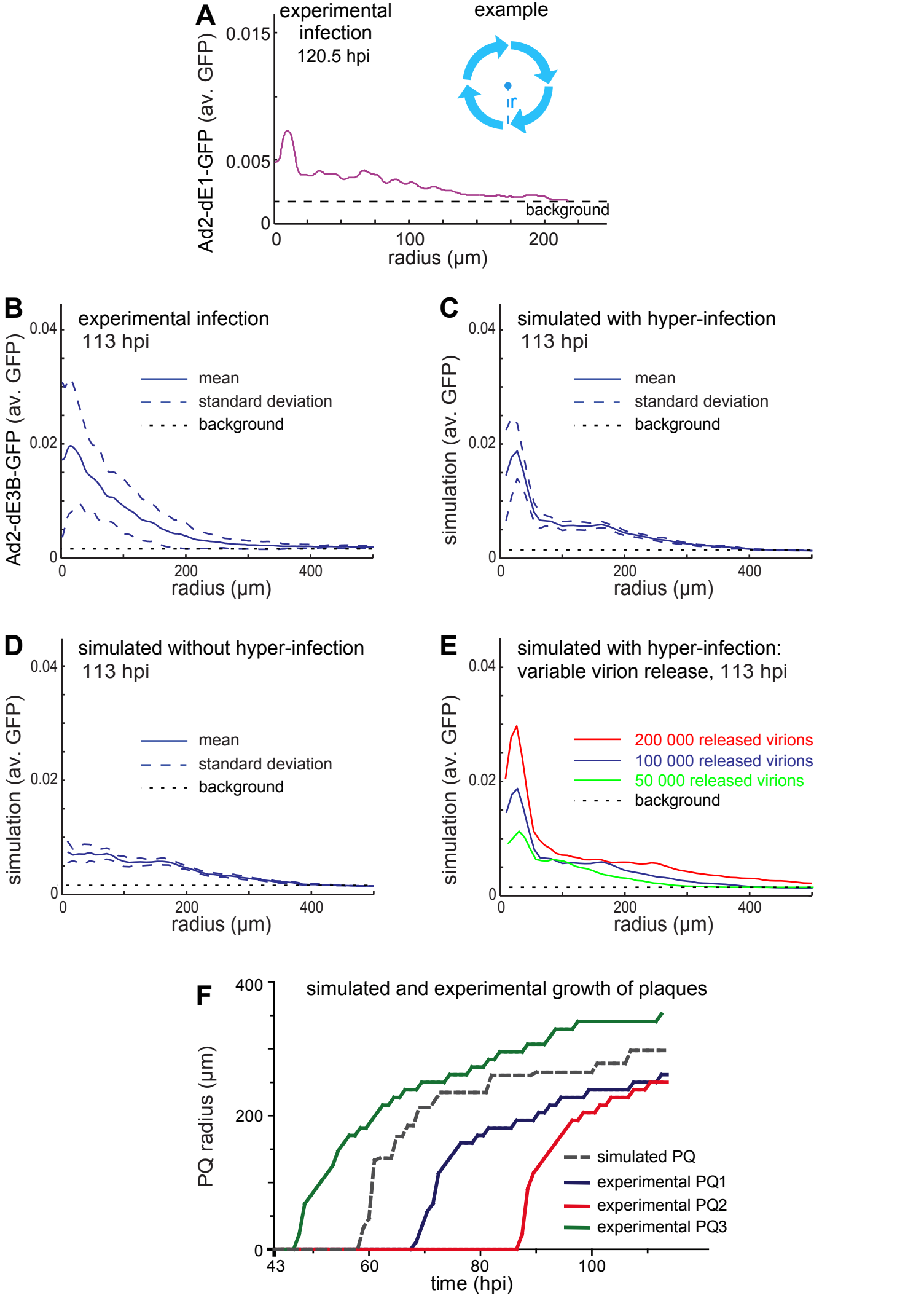
A
experimental infection
120.5 hpi
example
Ad2-dE1-GFP (av. GFP)
0.015
0.005
0
background
0
100
200
radius (μm)
B
experimental infection
113 hpi
mean
standard deviation
background
Ad2-dE3B-GFP (av. GFP)
0.04
0.02
0
0
200
400
radius (μm)
C
simulated with hyper-infection
113 hpi
mean
standard deviation
background
simulation (av. GFP)
0.04
0.02
0
0
200
400
radius (μm)
D
simulated without hyper-infection
113 hpi
mean
standard deviation
background
simulation (av. GFP)
0.04
0.02
0
0
200
400
radius (μm)
E
simulated with hyper-infection:
variable virion release, 113 hpi
200 000 released virions
100 000 released virions
50 000 released virions
background
simulation (av. GFP)
0.04
0.02
0
0
200
400
radius (μm)
F
simulated and experimental growth of plaques
PQ radius (μm)
400
200
0
43
60
80
100
time (hpi)
simulated PQ
experimental PQ1
experimental PQ2
experimental PQ3

Supplemental Material

Supplemental figures, movies and legends

Fig. S1

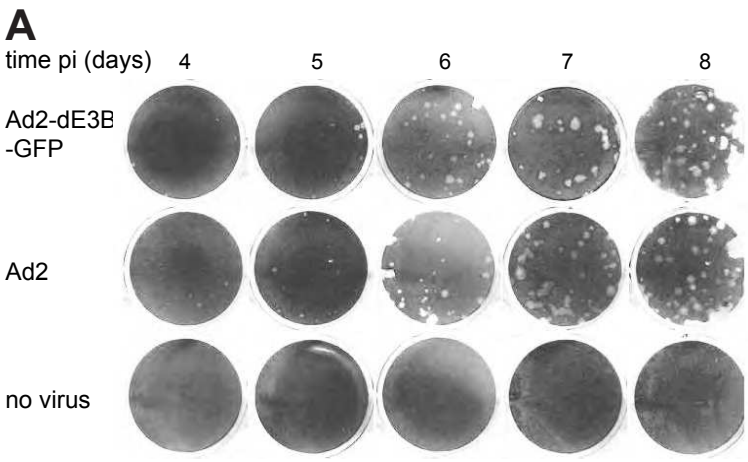

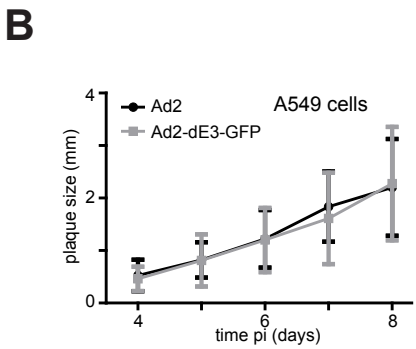

time pi (days)	4	5	6	7	8
plaque (no)					
Ad2-dE3B-GFP	16	30	40	41	45
Ad2	16	34	37	52	46

Fig. S1: Ad2-dE3B-GFP and Ad2 give rise to similar plaques on HLC-A549 cells

Cells grown in monolayers on 12-well plates were inoculated with virus at 37°C for 1 h, inoculum was removed and cells covered with agar overlay in growth medium as described earlier [1]. Four to eight days post infection (dpi), cells were fixed and stained with crystal violet. Panel A shows scans of stained plates and uninfected control cells. Panel B shows a plot of average plaque diameters including standard deviations as a function of infection time using ImageJ software for fitting circles of respective diameters to the plaques identified in the crystal violet stained cells.

Fig. S2

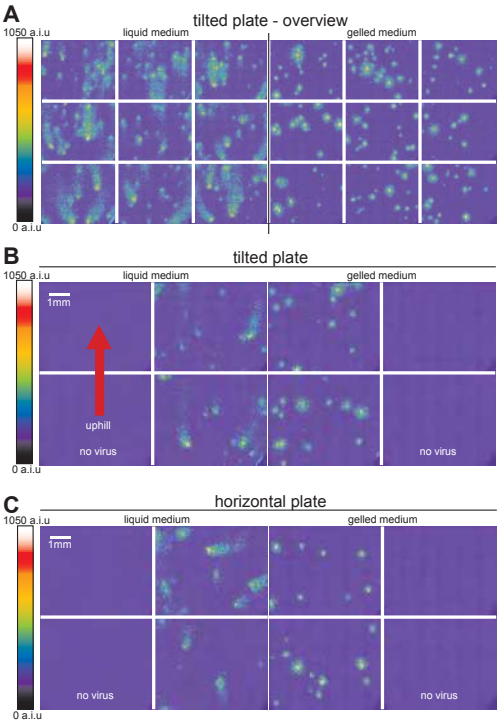

Fig. S2: Advection and diffusion control the shape of Ad2-dE3B-GFP plaques in liquid medium

HLC-A549 cells were inoculated with Ad2-dE3B-GFP in growth medium at 37°C for 2 h, washed in medium, and overlaid with liquid medium or medium containing 0.6% agarose (gelled medium). Plates were either tilted by 37° derived from arctan of the stand height and the plate width (measured with mm precision), or left horizontal and imaged for GFP analyses 5 dpi without fixation as described in Materials and Methods. Panel A shows an overview of a tilted plate, and B and C show close ups of tilted or horizontal plates. GFP intensities are indicated as arbitrary linear intensity units (a.i.u.) in pseudo-colours on the left. The Hoechst 33342 signal indicating cell nuclei is not shown here.

Note that that there is no preferred directionality of the plaque comets in the horizontal plate, while the comets in the tilted plate are largely aligned ‘uphill’ presumably under the influence of advection. The cells overlaid with agarose did not show comet plaques, neither tilted nor horizontal. We conclude that comet plaques are results of convection composed of advection and diffusion, while the symmetrical plaques under agarose are the result of diffusion.

Fig. S3

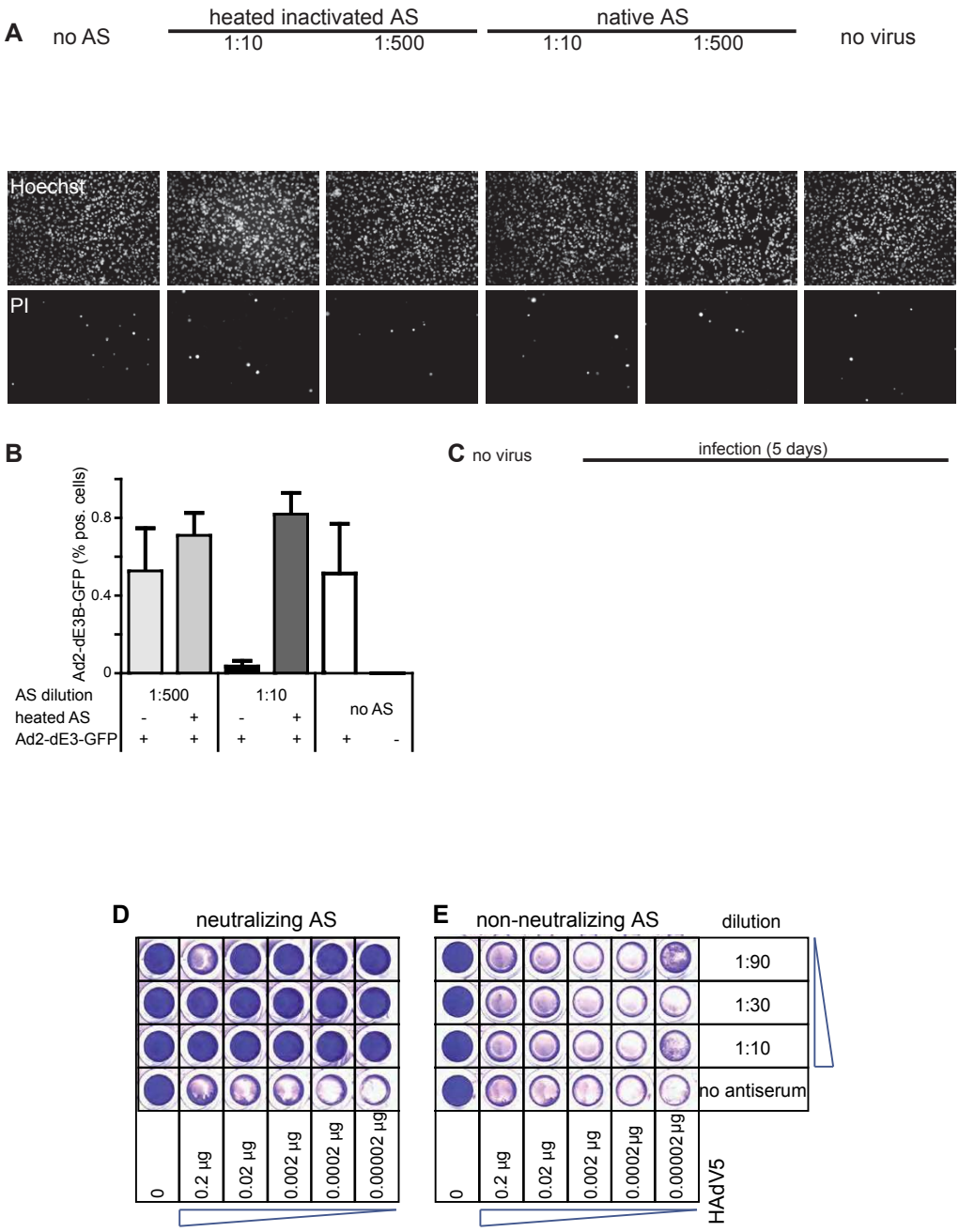

Fig. S3: Anti-HAdV-2/5 antiserum blocks infection and virus spreading

Ad2-dE3B-GFP or control medium was added to HLC-A549 cells in 384 well monolayers at 37°C for 1 h in presence or absence of native or heat-inactivated anti-adenovirus antiserum (AS). Cells were imaged in the GFP and the Hoechst 33342 channels 20 hpi (panel A), and the fraction of infected cells quantified using

CellProfiler (v2.0) based on Hoechst (cell nuclei) and GFP infection signals. The results show dose-dependent virus neutralization by the AS. Panel C shows GFP signals of infected cells in plate overviews 5 dpi, in presence or absence of different concentrations of AS. These data demonstrate blocking effects by the neutralizing AS on plaque formation. Panels D and E show end point titration assays with multiple rounds of infection, confirming the neutralization efficacy of AS. Various amounts of Ad5 were incubated with different dilutions of neutralizing AS (**D**), or non-neutralizing boiled AS (**E**) in 50 µl of medium in 96 well plates at room temperature for 15 to 30 min, followed by addition of HLC-A549 cells. The cells were fixed, and stained with crystal violet (dark color) 7 dpi. Wells where cells were detached or lysed by the virus appear transparent.

Fig. S4

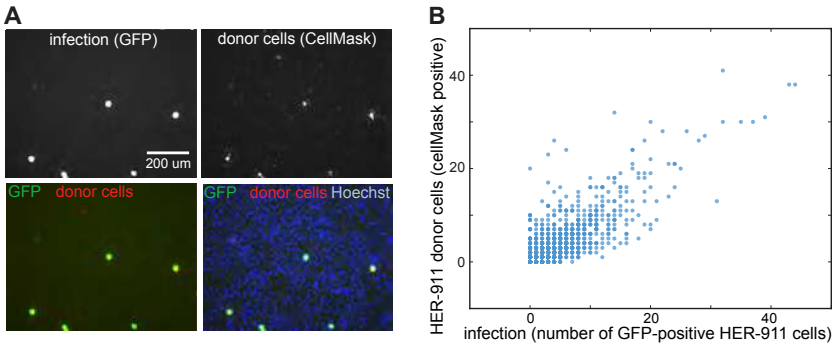

Fig. S4: Co-culture of infected HER-911 and uninfected HLC-A549 cells reveals virus spreading in single round infections

HER-911 cells were infected with Ad2-dE1-GFP, stained with CellMask red live dye, detached and seeded onto uninfected HLC-A549 cells. Cells were fixed 22 h post seeding and stained with the DNA-dye Hoechst. (**A**) Imaging of GFP (infection) and CellMask red live dye (HER-911) indicates that the donor HER-911 cells are positive for GFP. Panel (**B**) shows a plot of the number of CellMask positive cells and the number of GFP-positive cells, indicating a strong correlation between the two signals.

Fig. S5

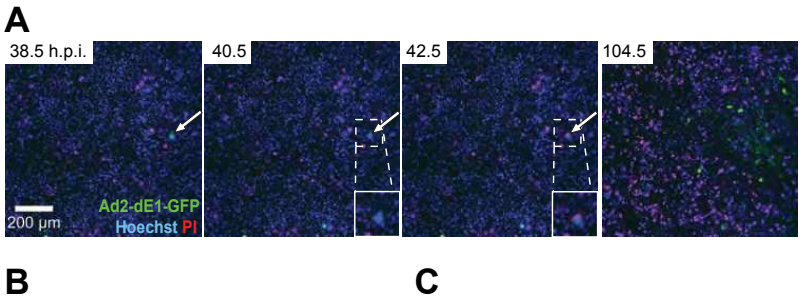

Fig. S5: Semi-solid agarose medium restricts advection of Ad2-dE1-GFP in absence of second round of infection

(**A**) Lysis of a HER-911 donor cell among uninfected HLC-A549 cells. Color composites show GFP (green), Hoechst 33342 (blue) and propidium iodide (red). Roughly spherical plaques seen in HLC-A549 cells under semi-solid 0.6 % agarose medium (**B**), and elongated plaques in aqueous medium (**C**). Multiple images (6x6) were stitched to give an overview impression. Each square image represents an imaging site from a single well taken in a time-lapse automated fluorescence microscopy experiment. Bar = 1 mm. Time points in the upper left corners are designated in hpi.

Fig. S6

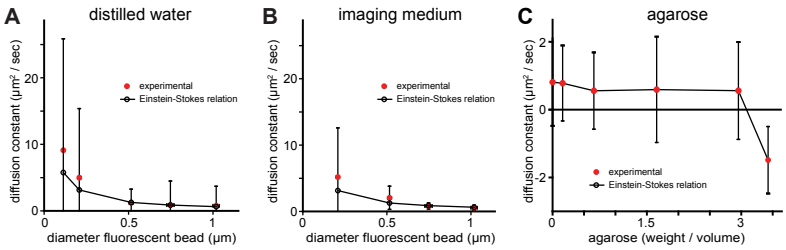

Fig. S6: Measurement of diffusion constants from fluorescent beads

Graphical representation of the diffusion constants for different sized fluorescent polymer beads in distilled water (**A**) or imaging medium (**B**). Diffusion constants of various sized fluorescent beads were measured experimentally, or calculated using Einstein-Stokes relation (equation 2 in the main text). (**C**) Diffusion constants of Ad2-atto565 were experimentally measured in imaging medium containing different concentrations of agarose yielding semi-solid medium. Error bars represent standard deviations of the mean diffusion constants of fluorescent beads obtained using moment scaling spectrum slopes [2] of Brownian motion trajectories tracked in 50 independent measurements (movies) for each condition.

Figure S7

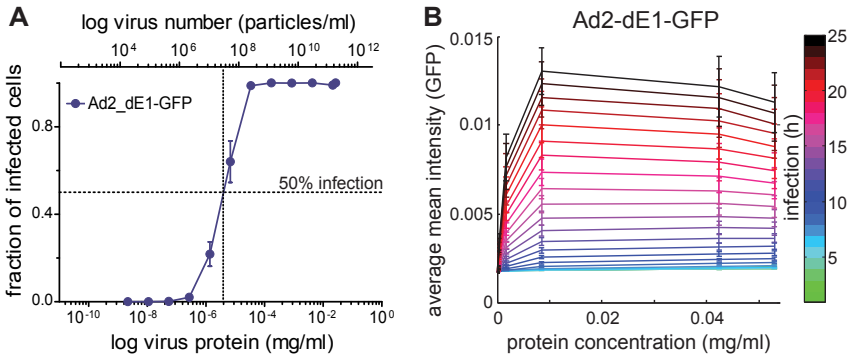

Fig. S7: Infection probability and GFP expression kinetics depend on the dose of Ad2-dE1-GFP

Multi-site time-lapse imaging of HLC-A549 cells infected with different amounts of Ad2-dE1-GFP was performed, and analyzed for infection probability depending on the dose of input virus. CellProfiler software was used to classify infected and uninfected cells. (**A**) The fractions of infected cells depend on amounts of virus input shown as virus protein concentration and theoretical number of adenovirus particles. (**B**) GFP intensities averaged per well as a measure of infection are plotted for each virus concentration (mg protein per ml) at the time points indicated by the color scale on the right side of the panel.

Movie_S1

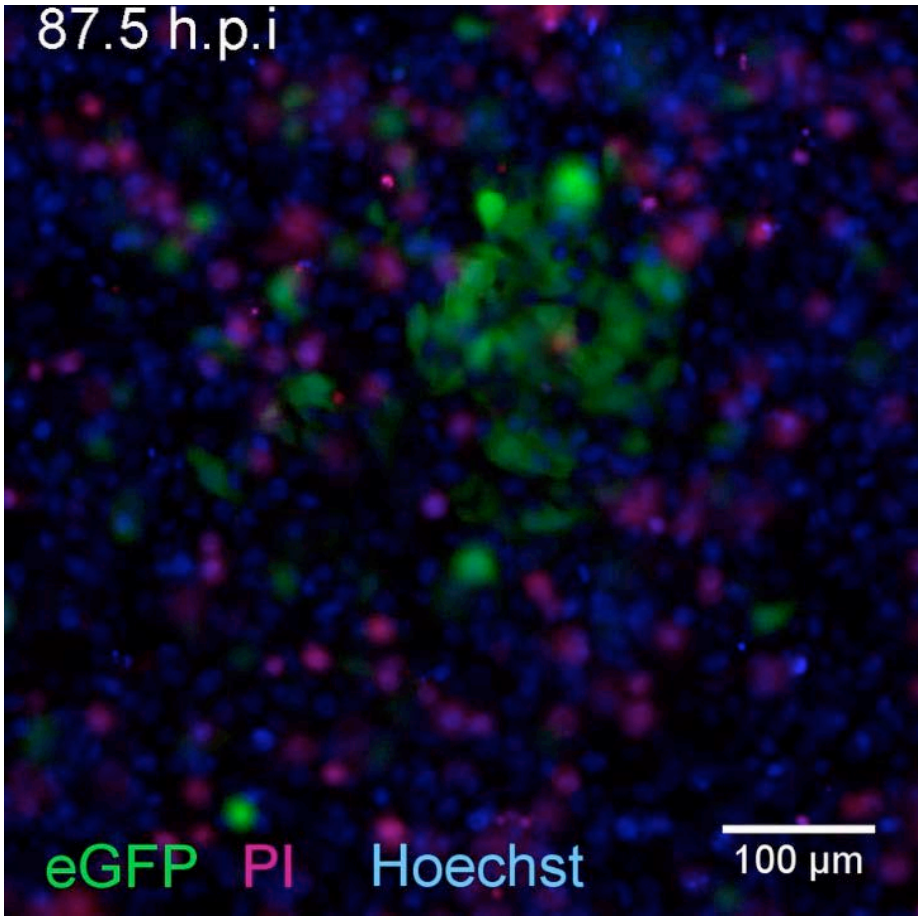

Movie S1: The formation of plaques occurs after cell lysis

Human lung carcinoma A549 (HLC-A549) cells were cultivated in monolayers, inoculated with highly diluted purified Ad2-dE3B-GFP (10^{-7} mg virus protein in 200 µl cell culture medium) and imaged for GFP expression by multi-site time-lapse fluorescence microscopy. The sporadic occurrence of a small fraction of GFP-positive cells was observed before 44.5 hpi. Note that GFP behaves as a soluble protein and freely equilibrates in the cytosol and the nucleus [3]. At 2-3 dpi, circular zones of GFP-positive infected cells developed around some of the initially infected cells. An infected cell (GFP positive, green) became positive for propidium iodide dye (PI) after disappearance of the GFP signal, which indicated cell lysis. This is followed by the formation of an SP.

Movie_S2

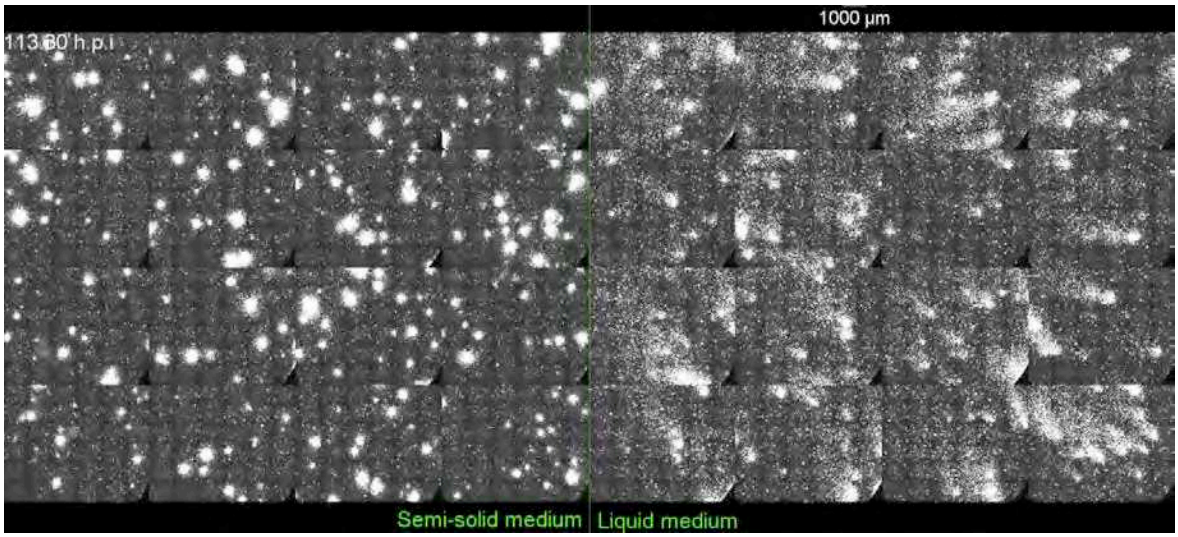

Movie S2: Semi-solid medium restricts advection and leads to the formation of circular plaques

Time-lapse microscopy revealed the influence of a semi-solid medium gelled 0.6% agarose (movie on the left side) on the shape of plaques, compared to the liquid medium (movie on the right side). Multiple sites and multiple wells were stitched together to yield overview movies.

Movie_S3

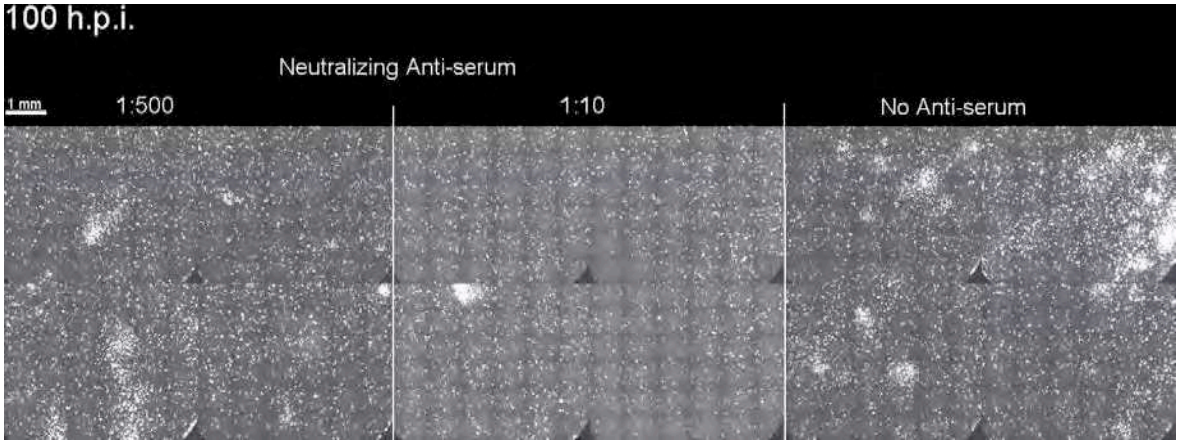

Movie S3: Neutralizing anti-Ad2/5 antiserum blocks the formation of plaques by Ad2-dE3B-GFP

Time-lapse microscopy revealed a dose-dependent spreading arrest by a neutralizing anti-Ad2/5 antiserum. The initial infection occurred with 10^{-6} mg/ml of Ad2-dE3B-GFP. Low-resolution overview images of stitched multiple sites and multiple wells are shown. The montages reveal the arrest in formation of plaques recognized as GFP expressing cells (gray scale signals).

Movie_S4

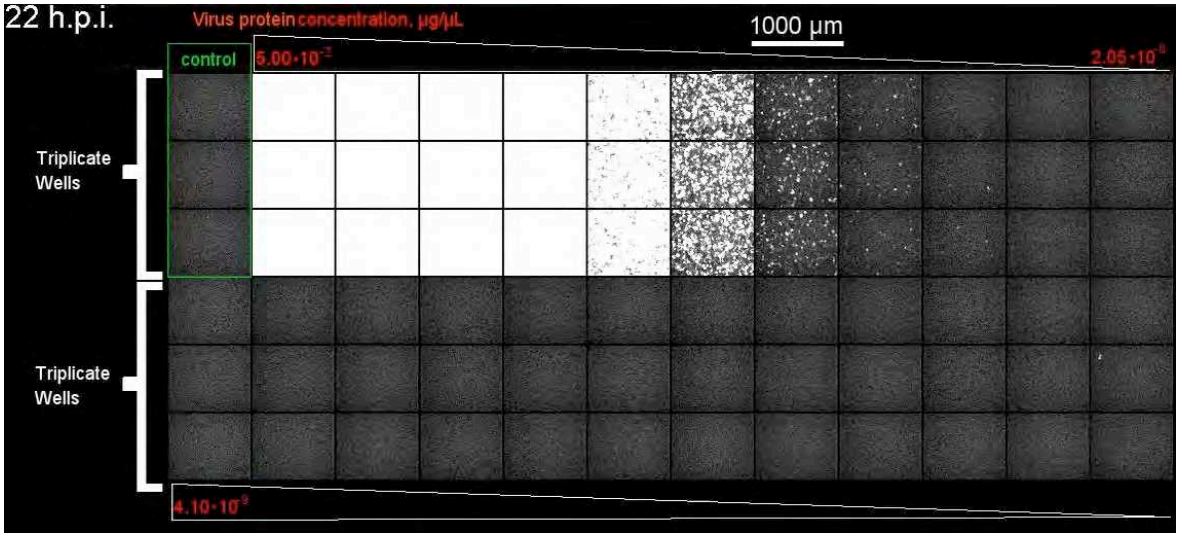

Movie S4: GFP expression kinetics depends on the dose of input Ad2-dE3B-GFP

Multi-site time-lapse imaging of HLC-A549 cells infected with different amounts of Ad2-dE3B-GFP virus shows decreasing levels of infection as the amounts of input virus decrease from left to right and from the upper to the lower row of triplicate samples. Each square image represents an imaging site from a well containing 200 µl of samples. Triplicates represent different wells infected with the same amounts of virus. The first three control wells were not infected.

Movie_S5

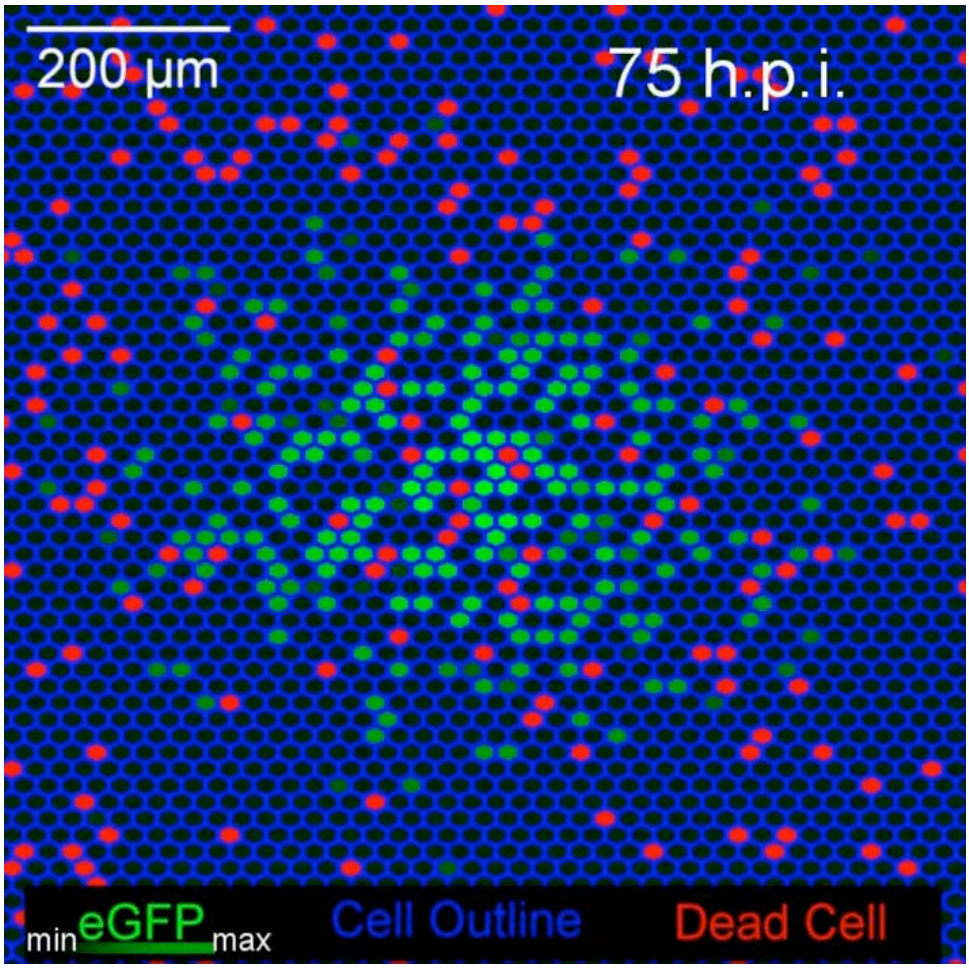

Movie S5: Simulation output from the hybrid model encompassing cellular automaton - particle strength exchange (CA-PSE)

The cells for the hexagon-based CA are outlined in blue and dead cells in red. Infected cells are denoted in green, where high green intensities reflect high levels of infection, and low intensities low infections. The animation starts 1 hpi, and has a temporal resolution of 1 h per frame.

Supplemental References

1. Greber UF, Willetts M, Webster P, Helenius A (1993) Stepwise dismantling of adenovirus 2 during entry into cells. Cell 75: 477-486.
2. Ewers H, Smith AE, Sbalzarini IF, Lilie H, Koumoutsakos P, et al. (2005) Single-particle tracking of murine polyoma virus-like particles on live cells and artificial membranes. Proc Natl Acad Sci U S A 102: 15110-15115.
3. Tsien RY (1998) The green fluorescent protein. Annu Rev Biochem 67: 509-544.